An optimally convergent smooth blended B-spline construction for semi-structured quadrilateral and hexahedral meshes

Koh, Kim Jie ; Toshniwal, Deepesh ; Cirak, Fehmi

DOI
10.1016/j.cma.2022.115438

Publication date
2022

Document Version
Final published version

Published in
Computer Methods in Applied Mechanics and Engineering

Citation (APA)
Koh, K. J., Toshniwal, D., & Cirak, F. (2022). An optimally convergent smooth blended B-spline construction for semi-structured quadrilateral and hexahedral meshes. *Computer Methods in Applied Mechanics and Engineering*, *399*, 1-28. Article 115438. https://doi.org/10.1016/j.cma.2022.115438

Available online at www.sciencedirect.com
ScienceDirect
Comput. Methods Appl. Mech. Engrg. 399 (2022) 115438
Computer methods in applied mechanics and engineering
www.elsevier.com/locate/cma

An optimally convergent smooth blended B-spline construction for semi-structured quadrilateral and hexahedral meshes

Kim Jie Koh[a], Deepesh Toshniwal[b], Fehmi Cirak[a,*]

[a] *Department of Engineering, University of Cambridge, Cambridge, CB2 1PZ, UK*
[b] *Delft Institute of Applied Mathematics, TU Delft, 628 XE Delft, The Netherlands*

Received 9 November 2021; received in revised form 17 July 2022; accepted 18 July 2022
Available online xxxx

Abstract

Easy to construct and optimally convergent generalisations of B-splines to unstructured meshes are essential for the application of isogeometric analysis to domains with non-trivial topologies. Nonetheless, especially for hexahedral meshes, the construction of smooth and optimally convergent isogeometric analysis basis functions is still an open question. We introduce a simple partition of unity construction that yields smooth blended B-splines, referred to as SB-splines, on semi-structured quadrilateral and hexahedral meshes, i.e. on mostly structured meshes with sufficiently separated unstructured regions. To this end, we first define the mixed smoothness B-splines that are C^0 continuous in the unstructured regions of the mesh but have higher smoothness everywhere else. Subsequently, the SB-splines are obtained by smoothly blending in the physical space the mixed smoothness B-splines with Bernstein bases of equal degree. One of the key novelties of our approach is that the required smooth weight functions are assembled from the available smooth B-splines on the unstructured mesh. The SB-splines are globally smooth, non-negative, have no breakpoints within the elements and reduce to conventional B-splines away from the unstructured regions of the mesh. Although we consider only quadratic mixed smoothness B-splines in this paper, the construction generalises to arbitrary degrees. We demonstrate the excellent performance of SB-splines studying Poisson and biharmonic problems on semi-structured quadrilateral and hexahedral meshes, and numerically establishing their optimal convergence in one and two dimensions.

Keywords: Isogeometric analysis; B-splines; Smooth splines; Quadrilateral meshes; Hexahedral meshes

1. Introduction

The smoothness of spline basis functions is vital in the isogeometric analysis of problems with higher-order partial differential equations. For instance, gradient-theories of elasticity and plasticity [1–5], phase-field modelling of sharp interfaces [6–8] and Kirchhoff–Love type plate and shell models [9–12] and their extensions [13,14] all lead to higher-order partial differential equations. Since its inception, isogeometric analysis brought about a revival of such theories mainly because of the ease of discretising higher-order partial differential equations using smooth spline basis functions. In particular, smooth basis functions avoid the introduction of (non-physical) extra degrees of

* Corresponding author.
E-mail address: f.cirak@eng.cam.ac.uk (F. Cirak).

https://doi.org/10.1016/j.cma.2022.115438
0045-7825/

Table 1
Summary of the terminology and symbols used in this paper. Note that this terminology, in particular, the usage of *blending* or *blended* is not uniform across the isogeometric analysis and geometric design literature.

Terminology	Definition
Mixed B-splines, $\boldsymbol{B}(\boldsymbol{x})$	B-splines of mixed smoothness.
Blending	Combination of different basis functions using weight functions.
SB-splines, $\boldsymbol{N}(\boldsymbol{x})$	Smooth blended splines obtained by the proposed construction.

freedom and promise a better integration with common computer-aided design representations. However, standard spline basis functions, including B-splines, NURBS and box-splines, are defined only on structured meshes and must be suitably extended for domains with non-trivial topology. For instance, multivariate B-splines are defined only on structured quadrilateral and hexahedral meshes in 2D and 3D, respectively. Most industrial complex geometries cannot be parametrised with a structured mesh so that a limited number of singularities on the surface or inside the volume must be introduced [15–23]. These singularities manifest themselves as extraordinary vertices and edges in the mesh, see Fig. 1. For a hexahedral mesh, an interior vertex is extraordinary if it is not incident to 8 hexahedra, and an interior edge is extraordinary if it is not incident to 4 hexahedra. Similarly, an interior vertex is extraordinary for a quadrilateral mesh if it is not incident to 4 quadrilaterals. The construction of smooth splines which generalise or extend B-splines to unstructured meshes is currently a very active area of research in isogeometric analysis.

In computer-aided design numerous constructions have been proposed to deal with extraordinary vertices in a surface mesh, including geometrically G^k and parametrically C^k continuous constructions [24–33], subdivision surfaces [34–40], macro-elements [41–43] and manifold constructions [44–50]. There are, however, a very limited number of constructions for volume meshes, including [51–56]; most likely because conventional computer-aided design representations do not require a volume parametrisation. As widely reported, most constructions from computer-aided design lead in isogeometric analysis to suboptimally convergent finite elements, especially when applied to higher-order partial differential equations; see the discussion in [29]. There are, however, constructions for semi-structured quadrilateral meshes, including [30,32,38,48,49], which yield optimal or nearly optimal convergence rates. In contrast, there are no B-spline based optimally convergent smooth constructions for unstructured hexahedral meshes. Currently, optimality is achieved by either reducing continuity to C^0 around extraordinary features [56–58], combining B-splines with meshless approximants [59] or resorting to non-standard spline definitions [60]. The first approach is not suitable for higher-order partial differential equations whereas the latter approaches lead to schemes that are usually computationally costly.

In this paper, we derive a computationally efficient, easy to construct and optimally convergent extension of B-splines to semi-structured quadrilateral and hexahedral meshes. We dub the new basis functions *SB-splines*; see Table 1 for the terminology used throughout this paper. Although we consider only quadratic B-splines, the presented ideas should carry over to arbitrary degrees. To begin with, we determine on the given unstructured mesh a set of B-splines of mixed smoothness following the construction for quadrilateral meshes in Toshniwal [61]. The mixed B-splines are C^0 continuous around extraordinary features, i.e. extraordinary vertices (in 2D and 3D) and extraordinary edges (in 3D), but are C^1 smooth everywhere else. Subsequently, we use the partition of unity method of Melenk and Babuška [62] to blend the mixed B-splines $\boldsymbol{B}(\boldsymbol{x})$ with tensor-product Bernstein basis functions $\boldsymbol{Q}(\boldsymbol{x})$ of equal degree. To this end, a set of smooth weight, or partition of unity, functions $w^B(\boldsymbol{x})$ and $w^Q(\boldsymbol{x})$ are defined to blend both types of basis functions. A key novelty of our approach is that the blending function $w^B(\boldsymbol{x})$ is assembled from the mixed B-splines on the unstructured mesh, by excluding the C^0 ones, so that $w^Q(\boldsymbol{x}) := 1 - w^B(\boldsymbol{x})$. Consequently, the weight functions $w^B(\boldsymbol{x})$ and $w^Q(\boldsymbol{x})$ are C^1 smooth and have their breakpoints at the element boundaries. On quadrilateral meshes with extraordinary vertices the SB-splines are simply given by the weighted basis functions $w^B(\boldsymbol{x})\boldsymbol{B}(\boldsymbol{x})$ and $w^Q(\boldsymbol{x})\boldsymbol{Q}(\boldsymbol{x})$. In hexahedral meshes, the extraordinary edges and vertices usually form a connected network as illustrated in Fig. 1(c); see also relevant work on hexahedral meshing [15–23]. That is, the weight function $w^Q(\boldsymbol{x}) = 1 - w^B(\boldsymbol{x})$ has a support over the entire network and is decomposed as $w^Q(\boldsymbol{x}) = \sum_i \sum_j w^P_{i,j}(\boldsymbol{x}) + \sum_j w^J_j(\boldsymbol{x})$ into locally supported weight functions. In brief, the support of one weight function $w^J_j(\boldsymbol{x})$ covers a region where more than two extraordinary edges meet, and the supports of the weight functions $w^P_{i,j}(\boldsymbol{x})$ are restricted to the remaining regions along the connecting extraordinary edge chains. We note for blending instead of the Bernstein basis $\boldsymbol{Q}(\boldsymbol{x})$ a different tensor-product basis or a triangular Bernstein–Bézier

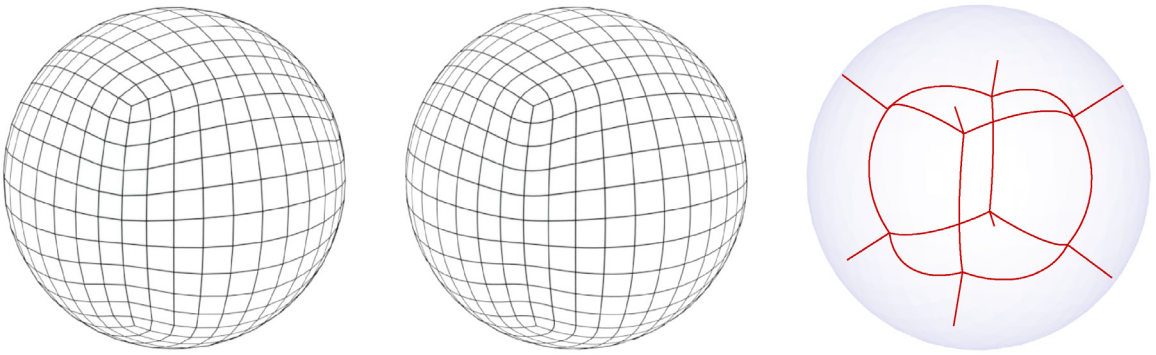

(a) Hexahedral mesh **(b)** Bézier mesh **(c)** Extraordinary edges and vertices

Fig. 1. Spherical domain discretised with a hexahedral mesh containing extraordinary edges and vertices. The Bézier mesh represents the physical domain.

basis can be considered. Similarly, in principle, differently constructed mixed smoothness B-splines $\boldsymbol{B}(\boldsymbol{x})$ could be used, including the enhanced smoothness B-splines presented in Buchegger and Jüttler [63], which are conceptually similar to the chosen mixed B-splines. However, the enhanced smoothness B-splines use nested refinement (leading to a more involved implementation) and exhibit optimal convergence only for extraordinary vertices with a valence 3 using uniform refinement.

The proposed approach uses, like the manifold-based constructions [46–50] and their variations [64–67], the partition of unity method to smoothly blend mixed B-splines with C^∞ continuous Bernstein basis functions. Unlike manifold-based constructions, the two types of basis functions are blended in the Euclidean ambient space, i.e. $\mathbb{R}^2$ in 2D and $\mathbb{R}^3$ in 3D. Thus, for blending we do not use an atlas consisting of charts and smooth transitions maps. Although it is easy to devise smooth transition maps for 2-manifolds, e.g. using conformal or characteristic maps [36,46], it is not clear how to construct them in $\mathbb{R}^3$. Circumventing the need for such a smooth atlas yields a conceptually and implementation-wise simpler approach and smooth basis functions with appealing properties. The SB-splines are obtained by blending polynomials defined on the parameter or ambient space and, hence, can be integrated very efficiently using standard Gauss–Legendre quadrature. Furthermore, the weight functions $w^B(\boldsymbol{x})$ and $w^Q(\boldsymbol{x})$ have minimal polynomial degree considering that they are assembled from B-splines and their complements to one.

The outline of this paper is as follows. To begin with, we briefly discuss in Section 2 the construction of SB-splines in 1D to introduce the key ideas and terminology used throughout the paper. Subsequently, we consider in Section 3 the construction of SB-splines on unstructured quadrilateral meshes with extraordinary vertices. We first review the mixed B-splines in Section 3.1 and then discuss the construction of SB-splines, in particular the weight functions, in Section 3.2. As explained in Section 3.2, it is straightforward to derive closed-form expressions of the new basis functions for use in existing isogeometric analysis implementations. In Section 4, we consider the construction of SB-splines on unstructured hexahedral meshes with extraordinary edges and vertices. After discussing the extension of mixed B-splines to hexahedral meshes in Section 4.1, we first introduce the notions of an *extraordinary prism* and *extraordinary joint* and discuss how to construct the respective weight and smooth basis functions in Section 4.2. Finally, we present in Section 5 several Poisson and biharmonic examples to confirm the convergence of the SB-splines. We study in particular the influence of the number of quadrature points and the valence of the extraordinary vertices on finite element convergence in 2D. Although we have not investigated the finite element convergence in 3D, we demonstrate the global C^1 continuity and excellent performance of the finite element solution on the same spherical domain as shown in Fig. 1. The paper is supplemented by four appendices that provide a proof of linear independence and discuss aspects of finite element discretisation, mesh refinement and an illustration of the treatment of arbitrary hexahedral meshes.

2. One-dimensional SB-splines

The proposed construction is best illustrated in the one-dimensional setting. Given is a domain $\Omega \subset \mathbb{R}$ with the parametrisation

$$x(\xi) = \sum_{i=1}^{n_B} B_i(\xi) x_i \quad \text{with } \xi \in \hat{\Omega} := [0, 1]\,, \tag{1}$$

where $B_i(\xi)$ are the univariate B-splines of degree $p_B \geq 2$ and x_i are the coordinates of the control points. As mentioned earlier, in higher dimensions we will focus solely on the case $p_B = 2$. The B-splines $B_i(\xi)$ are defined on the parametric domain $\hat{\Omega}$ with the parametric coordinate ξ. For the sake of illustration, they are chosen to be C^0 continuous at the break point ξ_{ep} and C^{p_B-1} continuous at every other break point. Hence, the point with the coordinate $x_{\text{ep}} := x(\xi_{\text{ep}})$ is an extraordinary point.

Assuming that the parametrisation $x(\xi)$ is, as usual, bijective, the push-forward of the basis functions on the physical domain Ω are given by

$$B_i(x) = B_i(\xi) \circ x(\xi)^{-1}\,. \tag{2}$$

For later reference, the basis functions on the physical domain Ω are collected in the array

$$\boldsymbol{B}(x) = \begin{pmatrix} B_1(x) & \dots & B_{n_B}(x) \end{pmatrix}^{\mathsf{T}}\,. \tag{3}$$

In the neighbourhood of the extraordinary point x_{ep}, we aim to blend the B-splines $\boldsymbol{B}(x)$ with a second polynomial basis defined only over the blending domain $\Omega^Q \subset \Omega$. The second basis is, without loss of generality, throughout this paper a Bernstein basis with the basis functions

$$\boldsymbol{Q}(x) = \begin{pmatrix} Q_1(x) & \dots & Q_{n_Q}(x) \end{pmatrix}^{\mathsf{T}}\,, \tag{4}$$

where $n_Q = p_Q + 1$ and p_Q is the polynomial degree of the Bernstein basis.

For blending together the two sets of basis functions, we choose a weight function $w^Q(x)$ with $\operatorname{supp} w^Q(x) = \Omega^Q$ and its complement to one $w^B(x)$, i.e.,

$$w^Q(x) + w^B(x) \equiv 1 \quad \forall x \in \Omega\,. \tag{5}$$

Such weight functions can be chosen in many different ways. In the proposed construction, we assemble the weight function $w^B(x)$ from the B-splines $B_i(x)$. In particular, with the index set $\mathcal{I} = \{i \mid B_i(x) \text{ is at most } C^0 \text{ at } x_{\text{ep}}\}$ and its complement $\mathcal{I}^{\complement}$, the weight function is given by

$$w^B(x) = \sum_{i \in \mathcal{I}^{\complement}} B_i(x)\,. \tag{6}$$

The so-assembled weight functions have the following properties.

Proposition 1. *The weight functions $w^B(x)$ and $w^Q(x)$ are at least C^1 smooth, piecewise polynomials in the parameter space, have local support and form a partition of unity.*

Finally, using the above set of weight and basis functions, we define the smooth blended B-splines, or SB-splines, as

$$\boldsymbol{N}(x) = \begin{pmatrix} w^B(x)\boldsymbol{B}(x)^{\mathsf{T}} & w^Q(x)\boldsymbol{Q}(x)^{\mathsf{T}} \end{pmatrix}^{\mathsf{T}} = \begin{pmatrix} N_1(x) & \dots & N_{n_N}(x) \end{pmatrix}^{\mathsf{T}}\,, \tag{7}$$

where $n_N = n_B + n_Q$. Evidently, the smoothness, the support size and the polynomial degree of the SB-splines depend on the properties of $\boldsymbol{B}(x)$, $\boldsymbol{Q}(x)$, $w^B(x)$ and $w^Q(x)$. Critical for the smoothness properties of the SB-splines is the choice of the weight function $w^B(x)$.

Proposition 2. *The SB-splines $\boldsymbol{N}(x)$ are at least C^1 smooth, linearly independent, non-negative, have local support and form a partition of unity.*

The properties of smoothness, non-negativity, local support and partition of unity follow directly from the blending construction since both $\boldsymbol{B}(x)$ and $\boldsymbol{Q}(x)$ possess these properties. For the proof of linear independence, see Appendix A.

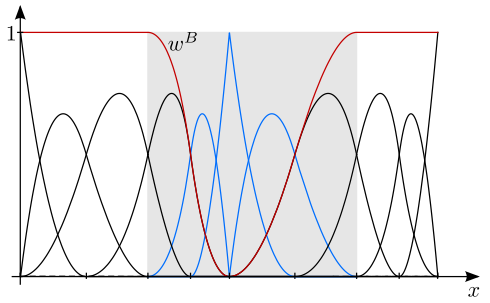

(a) $\boldsymbol{B}(x)$ in black and blue and $w^B(x)$ in red

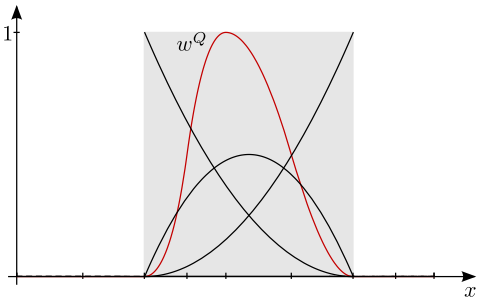

(b) $\boldsymbol{Q}(x)$ in black and $w^Q(x)$ in red

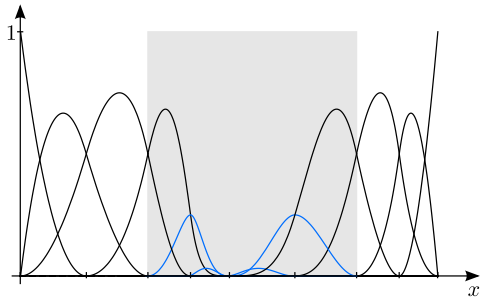

(c) $w^B(x)\boldsymbol{B}(x)$

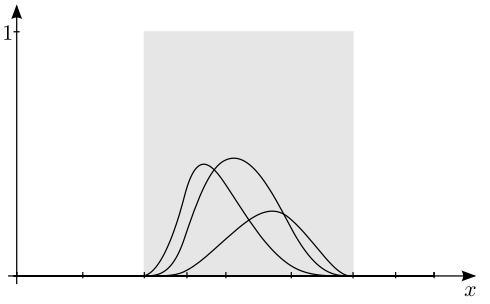

(d) $w^Q(x)\boldsymbol{Q}(x)$

Fig. 2. Blending of the mixed smoothness quadratic B-splines $\boldsymbol{B}(x)$ in (a) with the quadratic Bernstein basis functions $\boldsymbol{Q}(x)$ in (b). The non-uniform open knot vector for the B-splines $\boldsymbol{B}(x)$ has repeated knot values at the boundaries and at the extraordinary point at the centre of the physical domain Ω. In (a) the B-splines in blue are C^0 continuous at the extraordinary point. The blending domain Ω^Q is shaded in grey. The weight function $w^B(x)$ in (a) is the sum of the B-spline basis functions which are C^1 smooth at the extraordinary point. Its complement to one is the weight function $w^Q(x)$ in (b). (For interpretation of the references to colour in this figure legend, the reader is referred to the web version of this article.)

As a concrete example, Fig. 2 illustrates the blending of mixed smoothness quadratic B-splines $\boldsymbol{B}(x)$ with quadratic Bernstein basis functions $\boldsymbol{Q}(x)$. The physical domain Ω has at its centre an extraordinary point with C^0 continuity, introduced using a non-uniform open knot vector for $\boldsymbol{B}(x)$. Except at the extraordinary point the quadratic B-spline basis $\boldsymbol{B}(x)$ is C^1 smooth. The weight function $w^B(x)$ is assembled from B-splines $B_i(x)$ by excluding the ones which are at most C^0 smooth at the extraordinary point. Hence, the weight function $w^B(x)$ and, in turn, its complement $w^Q(x) = 1 - w^B(x)$ are intrinsically C^1 smooth. The blending domain Ω^Q is equal to the support of the weight function $w^Q(x)$. After determining the weight functions it is straightforward to compute the basis functions $N_i(x)$ depicted in Figs. 2(c) and 2(d), which are all C^1 smooth. We stress that a key aspect of our construction is that the weight function $w^B(x)$ is assembled from the smooth B-splines $\boldsymbol{B}(x)$. As apparent in Fig. 2(a), outside the blending region Ω^Q the weight function $w^B(x)$ is equal to one so that the SB-splines are equal to the standard B-splines.

Evidently, the proposed construction can be applied to B-splines of any degree. Fig. 3 illustrates the blending of mixed smoothness cubic B-splines and cubic Bernstein basis functions. The SB-splines depicted in Figs. 3(c) and 3(d) are C^1 continuous. In the next sections, we restrict our attention to $p_B = p_Q = 2$.

3. Two-dimensional quadratic SB-splines

We are given an unstructured quadrilateral mesh describing a domain $\Omega \subset \mathbb{R}^2$. The mesh consists of elements, i.e. quadrilateral faces, and their edges and vertices. We assume that all the vertices on the boundary of the mesh are regular, i.e. are incident to two elements, and all the extraordinary vertices within the mesh, i.e. vertices with other than four incident elements, are sufficiently separated as to be specified. If not the case, this can be achieved by successive quadrisection refinement of the mesh. The new vertices introduced during refinement are all regular so that the extraordinary vertices become more and more separated. In the following, without loss of generality, we

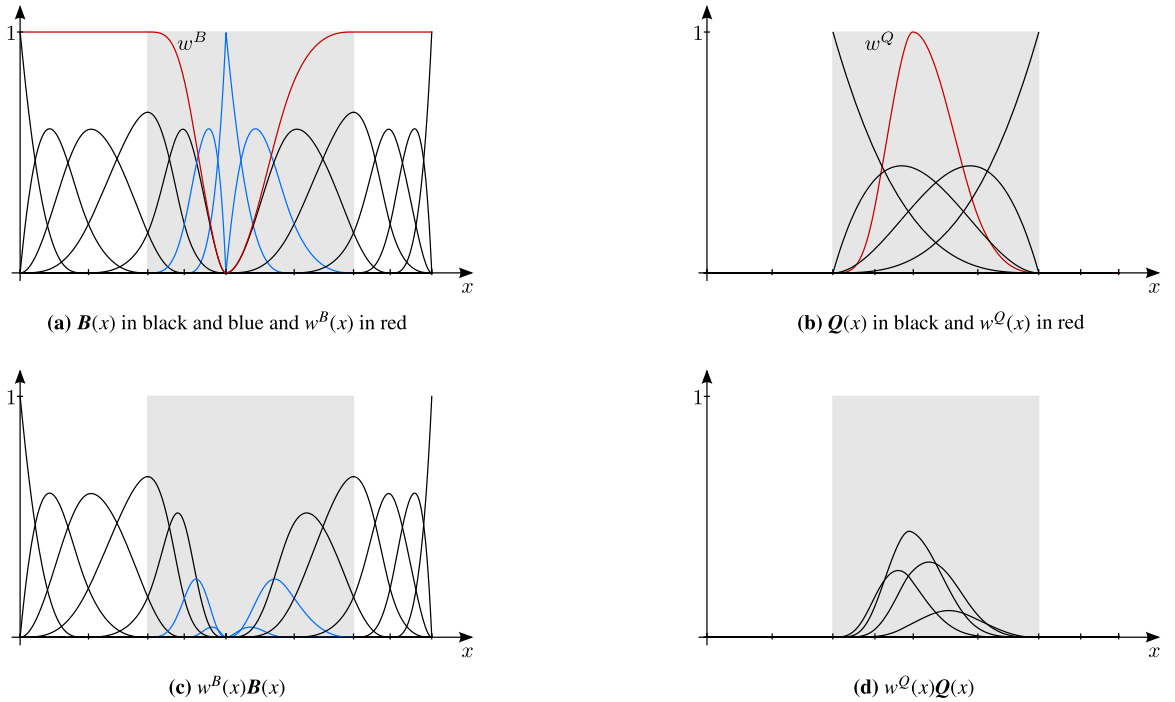

(a) $\boldsymbol{B}(x)$ in black and blue and $w^B(x)$ in red

(b) $\boldsymbol{Q}(x)$ in black and $w^Q(x)$ in red

(c) $w^B(x)\boldsymbol{B}(x)$

(d) $w^Q(x)\boldsymbol{Q}(x)$

Fig. 3. Blending of the mixed smoothness cubic B-splines $\boldsymbol{B}(x)$ in (a) with the cubic Bernstein basis functions $\boldsymbol{Q}(x)$ in (b). The non-uniform open knot vector for the B-splines $\boldsymbol{B}(x)$ has repeated knot values at the boundaries and at the extraordinary point at the centre of the physical domain Ω. In (a) the B-splines in blue are C^0 continuous at the extraordinary point. The blending domain Ω^Q is shaded in grey. The weight function $w^B(x)$ in (a) is the sum of the B-spline basis functions which are at most C^1 smooth at the domain centre. Its complement to one is the weight function $w^Q(x)$ in (b). (For interpretation of the references to colour in this figure legend, the reader is referred to the web version of this article.)

focus on bi-quadratic B-splines and assume that the mesh has a single extraordinary vertex of valence $v \neq 4$. In the (locally) structured regions of the mesh standard smooth tensor-product bi-quadratic B-splines can be defined. It is impossible to define such B-splines in the 1-neighbourhood of an extraordinary vertex due to the lack of a tensor-product mesh structure. A 1-neighbourhood of a vertex is formed by the union of the elements incident to the vertex. The n-neighbourhood is defined recursively as the union of all 1-neighbourhoods of all the vertices in the $(n-1)$-neighbourhood. With this definition at hand, we require that the 3-neighbourhoods of the extraordinary vertices in the considered mesh are disjoint.

3.1. Review of mixed B-splines

Although it is not possible to define a standard tensor-product B-spline basis on an unstructured mesh, it is possible to construct a B-spline basis of mixed smoothness, see Toshniwal [61]. The mixed B-splines are C^1 continuous away from the 1-neighbourhood of extraordinary vertices and are C^0 continuous along mesh edges incident to extraordinary vertices. That is, away from the 1-neighbourhood of extraordinary vertices the mixed B-splines are identical to tensor-product B-splines. On structured meshes there is a one-to-one correspondence between the bi-quadratic B-splines and elements (away from the boundaries). This is also the case for mixed B-splines. Hence, we can assign a control vertex to each element. The support of a mixed B-spline consists of all elements sharing a vertex with the respective element.

We represent the non-zero mixed B-splines within an element with bi-quadratic Bézier basis functions. The control vertices of the mixed B-splines are denoted with $\boldsymbol{x}_i \in \mathbb{R}^2$ and the ones of the Bézier basis functions with $\boldsymbol{c}_j \in \mathbb{R}^2$. The numbering of both sets of control vertices is given in Fig. 4(a). We define the mixed B-splines by first establishing the map from the control vertices $\boldsymbol{x}_i$ to $\boldsymbol{c}_j$. To this end, the Bézier control vertices are expressed as

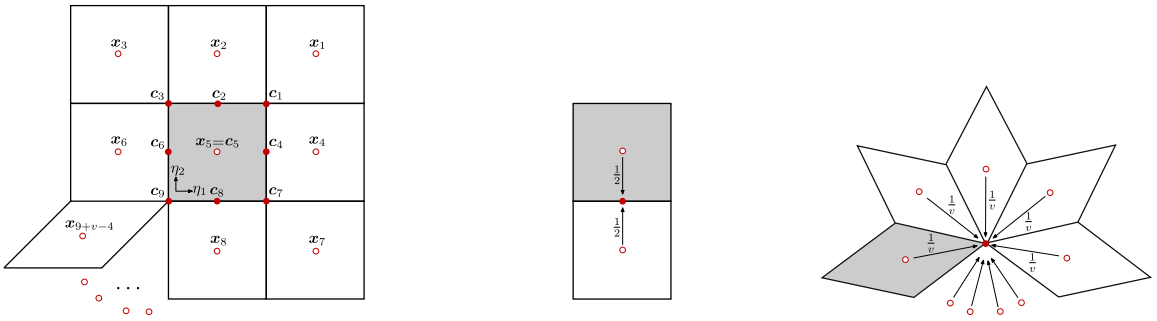

(a) Mixed B-spline & Bézier control vertices **(b)** Edge mask **(c)** Vertex mask for valence v

Fig. 4. Averaging masks for computing the bi-quadratic Bézier control vertices $\boldsymbol{c}_j$. The empty circles denote the mixed B-spline control vertices $\boldsymbol{x}_i$ and the solid circles the Bézier control vertices $\boldsymbol{c}_j$. The corner mask (c) for extraordinary vertices is a straightforward generalisation of the corner mask for ordinary vertex with $v = 4$. The masks (b) and (c) describe a bi-quadratic B-spline when an element's all vertices are regular.

linear combinations of the mixed B-spline control vertices. The corresponding weights can be graphically visualised with the masks shown in Figs. 4(b) and 4(c). The edge Bézier control vertices $\boldsymbol{c}_2$, $\boldsymbol{c}_6$, $\boldsymbol{c}_8$ and $\boldsymbol{c}_4$ are determined using the mask in Fig. 4(b) and the corner Bézier control vertices $\boldsymbol{c}_1$, $\boldsymbol{c}_3$, $\boldsymbol{c}_9$ and $\boldsymbol{c}_7$ using the mask in Fig. 4(c). The centre Bézier control vertex $\boldsymbol{c}_5$ has the same value as the mixed B-spline control vertex $\boldsymbol{x}_5$. Finally, the mapping of the mixed B-spline control vertices $\boldsymbol{x}_i$ to the Bézier control vertices $\boldsymbol{c}_j$ is given by

$$\begin{pmatrix} \boldsymbol{c}_1 \\ \boldsymbol{c}_2 \\ \boldsymbol{c}_3 \\ \boldsymbol{c}_4 \\ \boldsymbol{c}_5 \\ \boldsymbol{c}_6 \\ \boldsymbol{c}_7 \\ \boldsymbol{c}_8 \\ \boldsymbol{c}_9 \end{pmatrix} = \begin{pmatrix} \frac{1}{4} & \frac{1}{4} & 0 & \frac{1}{4} & \frac{1}{4} & 0 & 0 & 0 & \cdots & 0 \\ 0 & \frac{1}{2} & 0 & 0 & \frac{1}{2} & 0 & 0 & 0 & \cdots & 0 \\ 0 & \frac{1}{4} & \frac{1}{4} & 0 & \frac{1}{4} & \frac{1}{4} & 0 & 0 & \cdots & 0 \\ 0 & 0 & 0 & \frac{1}{2} & \frac{1}{2} & 0 & 0 & 0 & \cdots & 0 \\ 0 & 0 & 0 & 0 & 1 & 0 & 0 & 0 & \cdots & 0 \\ 0 & 0 & 0 & 0 & \frac{1}{2} & \frac{1}{2} & 0 & 0 & \cdots & 0 \\ 0 & 0 & 0 & \frac{1}{4} & \frac{1}{4} & 0 & \frac{1}{4} & \frac{1}{4} & \cdots & 0 \\ 0 & 0 & 0 & 0 & \frac{1}{2} & 0 & 0 & \frac{1}{2} & \cdots & 0 \\ 0 & 0 & 0 & 0 & \frac{1}{v} & \frac{1}{v} & 0 & \frac{1}{v} & \cdots & \frac{1}{v} \end{pmatrix} \begin{pmatrix} \boldsymbol{x}_1 \\ \boldsymbol{x}_2 \\ \boldsymbol{x}_3 \\ \boldsymbol{x}_4 \\ \boldsymbol{x}_5 \\ \boldsymbol{x}_6 \\ \boldsymbol{x}_7 \\ \boldsymbol{x}_8 \\ \vdots \\ \boldsymbol{x}_{9+v-4} \end{pmatrix} \quad \Rightarrow \quad \boldsymbol{c}_j = \sum_i M_{ji} \boldsymbol{x}_i \,. \tag{8}$$

Combining the Bézier basis functions $Q_j(\boldsymbol{\eta})$ of an element with the map (8) from the control vertices $\boldsymbol{x}_i$ to $\boldsymbol{c}_j$, we can define both a (local) parametrisation of the physical domain Ω and the mixed B-splines $B_i(\boldsymbol{x})$. Note that the Bézier basis functions $Q_j(\boldsymbol{\eta})$ are local to each element. Specifically, with the mixed B-spline control vertices $\boldsymbol{x}_i$ given in Fig. 4(a) and the map (8) the geometry parametrisation within the element corresponding to the control vertex $\boldsymbol{x}_5$ is given by

$$\boldsymbol{x}(\boldsymbol{\eta}) = \sum_{j=1}^{9} Q_j(\boldsymbol{\eta}) \boldsymbol{c}_j = \sum_{j=1}^{9} \sum_{i=1}^{9+v-4} Q_j(\boldsymbol{\eta}) M_{ji} \boldsymbol{x}_i \qquad \text{with } \boldsymbol{\eta} = (\eta_1,\, \eta_2) \in \square := [0,\,1] \times [0,\,1] \,. \tag{9}$$

This description also defines the mixed B-spline $B_5(\boldsymbol{x})$ associated to control vertex $\boldsymbol{x}_5$. According to (9), its preimage in the parametric domain is given by

$$B_5(\boldsymbol{\eta}) = \sum_{j=1}^{9} Q_j(\boldsymbol{\eta}) M_{j5} \tag{10}$$

such that

$$B_5(\boldsymbol{x}) = B_5(\boldsymbol{\eta}) \circ \boldsymbol{x}(\boldsymbol{\eta})^{-1} \,. \tag{11}$$

The B-splines $B_i(\boldsymbol{x})$ associated to the other control vertices in the mesh are obtained in the same way. See [61] for other properties of the mixed B-splines.

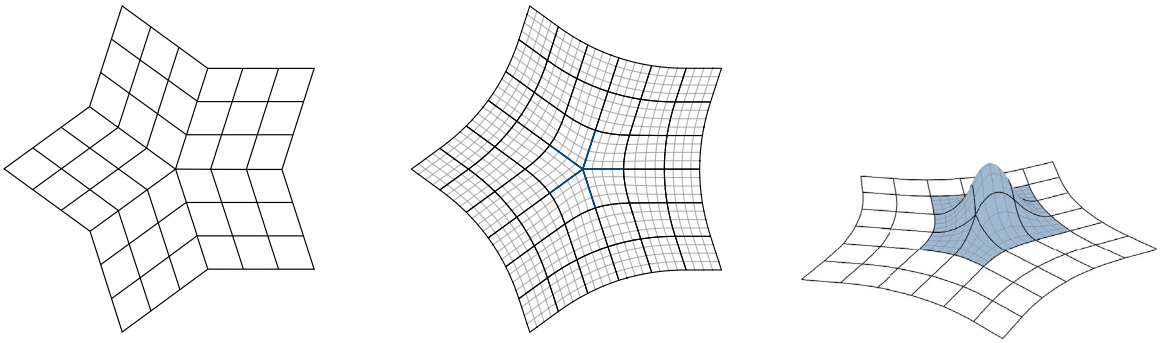

(a) Quadrilateral mesh **(b)** Bézier mesh **(c)** Basis function

Fig. 5. Unstructured quadrilateral mesh with only one extraordinary vertex with valence $v = 5$, its parametrisation and the graph of one of the corresponding basis functions. The thin lines in (b) and (c) indicate the parameter lines with either $\eta_1 = \text{const.}$ or $\eta_2 = \text{const.}$ In the 1-neighbourhood of the extraordinary vertex across the element edges, i.e. the blue edges in (b), the parametrisation is only C^0 continuous and everywhere else it is C^1 smooth. (For interpretation of the references to colour in this figure legend, the reader is referred to the web version of this article.)

As an example, the parametrised domain, i.e. Bézier mesh corresponding to the unstructured mesh in Fig. 5(a) with an extraordinary vertex with $v = 5$ is visualised in Fig. 5(b). The parametrisation is C^1 smooth in most parts of the domain as is suggested by the plotted parameter lines with either $\eta_1 = \text{const.}$ or $\eta_2 = \text{const.}$ It is C^0 continuous across the edges incident to the extraordinary vertex. For a control vertex in the 1-neighbourhood of the extraordinary vertex we obtain the basis function shown in Fig. 5(c). This basis function is only C^0 continuous across the edges incident to the extraordinary vertex, as can be inferred from the plotted parameter lines.

3.2. Construction of SB-splines

The construction of the blended C^1 smooth basis functions is analogous to 1D. First, we choose a weight function $w^B(\boldsymbol{x})$ and its complement to one $w^Q(\boldsymbol{x}) = 1 - w^B(\boldsymbol{x})$. The weight function $w^B(\boldsymbol{x})$ is assembled from the smooth mixed B-splines defined on the unstructured mesh. Importantly, the blending of the basis functions takes place in the physical domain Ω rather than the parametric domain of the basis functions. It is impossible to map every multi-dimensional physical domain with arbitrary topology onto a single parametric domain. This can be achieved only by introducing an atlas consisting of several charts with respective parametric domains and transition functions [48–50]. The definition of such smooth transition function on unstructured meshes is usually very challenging. Instead, constructing the weight functions on the physical domain sidesteps the need for an atlas and smooth transition functions.

As discussed in the preceding section smooth mixed B-splines $B_i(\boldsymbol{\eta})$ are defined only away from the 1-neighbourhood of an extraordinary vertex. Furthermore, the mixed B-splines $B_i(\boldsymbol{x})$ on the physical domain are obtained by mapping $B_i(\boldsymbol{\eta})$ from the reference element via the mapping $\boldsymbol{x}(\boldsymbol{\eta})^{-1}$, see (11). According to the chain rule of differentiation the smoothness of $B_i(\boldsymbol{x})$ relies both on the smoothness of $B_i(\boldsymbol{\eta})$ and $\boldsymbol{x}(\boldsymbol{\eta})^{-1}$. This implies that beyond the 1-neighbourhood of an extraordinary vertex most of the control vertices in its 2-neighbourhood belong to non-smooth mixed B-splines $B_i(\boldsymbol{x})$ as well, see Fig. 6(a).

We assemble the weight function $w^B(\boldsymbol{x})$ from the mixed B-splines $B_i(\boldsymbol{x})$ by excluding the ones belonging to the control vertices in the 2-neighbourhood of the extraordinary vertex, i.e. by excluding the mixed B-splines associated to all control vertices marked with a cross or a tick in Fig. 6(a). Although only the non-smooth mixed B-splines must be excluded, for ease of implementation we exclude some of the smooth mixed B-splines as well. The so-obtained smooth weight function $w^B(\boldsymbol{x})$ and its complement to one $w^Q(\boldsymbol{x}) = 1 - w^B(\boldsymbol{x})$ are depicted in Figs. 6(b) and 6(c), respectively. Evidently, both weight functions are C^1 smooth, bi-quadratic on the reference element domain $\square$ and $\operatorname{supp} w^Q(\boldsymbol{x})$ is comprised of the 3-neighbourhood of the extraordinary vertex.

Next, we choose a bi-quadratic Bernstein basis $\{Q_j(\boldsymbol{x})\}_{j=1}^{9}$ as the second basis for blending. These are defined on a different domain than the ones in (9); indeed, considering that the blending takes place in the physical domain Ω

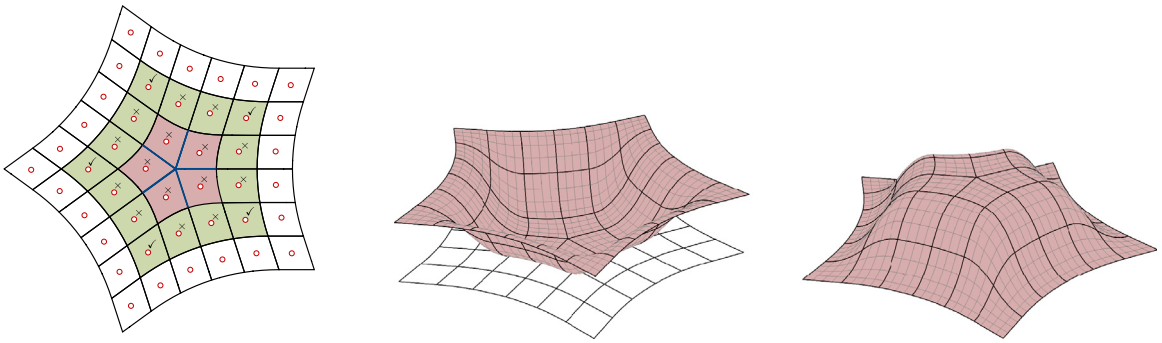

(a) Bézier mesh **(b)** $w^B(\boldsymbol{x})$ **(c)** $w^Q(\boldsymbol{x})$

Fig. 6. Smoothness of the mixed B-splines $B_i(\boldsymbol{x})$ and weight functions $w^B(\boldsymbol{x})$ and $w^Q(\boldsymbol{x})$. In (a) the mixed B-splines $B_i(\boldsymbol{x})$ are represented by the respective control vertices (empty circles). In addition, $B_i(\boldsymbol{x})$ that are C^1 and C^0 continuous across element edges in the 1-neighbourhood of the extraordinary vertex (blue edges) are labelled with ticks (✓) and crosses (×), respectively. In (b) the weight function $w^B(\boldsymbol{x})$ is assembled by excluding the mixed B-splines $B_i(\boldsymbol{x})$ belonging to the control vertices within the 2-neighbourhood of the extraordinary vertex. Its complement to one $w^Q(\boldsymbol{x}) = 1 - w^B(\boldsymbol{x})$ is shown in (c). (For interpretation of the references to colour in this figure legend, the reader is referred to the web version of this article.)

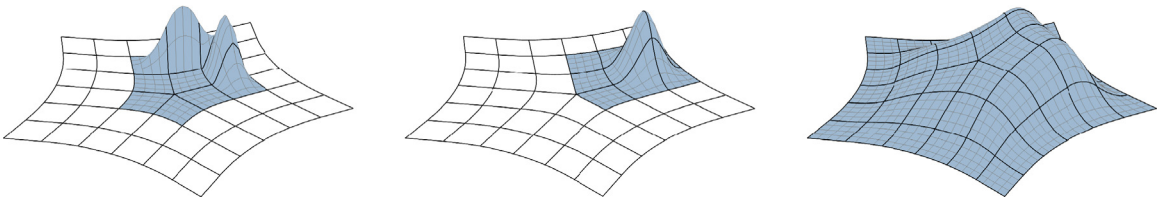

(a) $w^B(\boldsymbol{x})B_i(\boldsymbol{x})$ **(b)** $w^B(\boldsymbol{x})B_i(\boldsymbol{x})$ **(c)** $w^Q(\boldsymbol{x})Q_j(\boldsymbol{x})$

Fig. 7. Three of the obtained SB-splines $N_i(\boldsymbol{x})$. The SB-splines in (a) and (b) correspond to the non-smooth mixed B-splines $B_i(\boldsymbol{x})$ belonging to the control vertices in the 1- and 2-neighbourhoods, respectively. The SB-spline in (c) corresponds to one of the Bézier basis functions $Q_j(\boldsymbol{x})$.

the basis $\{Q_j(\boldsymbol{x})\}$ is defined in the physical domain with $\boldsymbol{x} \in \Omega$. To guarantee the positivity of the SB-splines, the domain of the Bernstein basis $\{Q_j(\boldsymbol{x})\}$ must enclose the blending domain Ω^Q, but can be chosen freely otherwise. As in 1D, the SB-splines are then defined by

$$\boldsymbol{N}(\boldsymbol{x}) = \begin{pmatrix} w^B(\boldsymbol{x})\boldsymbol{B}(\boldsymbol{x})^\mathsf{T} & w^Q(\boldsymbol{x})\boldsymbol{Q}(\boldsymbol{x})^\mathsf{T} \end{pmatrix}^\mathsf{T} \tag{12}$$

with

$$\boldsymbol{B}(\boldsymbol{x}) = \begin{pmatrix} B_1(\boldsymbol{x}) & \dots & B_{n_B}(\boldsymbol{x}) \end{pmatrix}^\mathsf{T}, \quad \boldsymbol{Q}(\boldsymbol{x}) = \begin{pmatrix} Q_1(\boldsymbol{x}) & \dots & Q_9(\boldsymbol{x}) \end{pmatrix}^\mathsf{T}. \tag{13}$$

The obtained basis functions $\boldsymbol{N}(\boldsymbol{x})$ are C^1 smooth. In Figs. 7(a) and 7(b) two of the basis functions $w^B(\boldsymbol{x})B_i(\boldsymbol{x})$ and in Fig. 7(c) one of the basis functions $w^Q(\boldsymbol{x})Q_j(\boldsymbol{x})$ are plotted.

In usual finite element implementations integrals are evaluated in a reference element domain $\square := [0, 1] \times [0, 1]$. To facilitate the element-based implementation of the proposed blended approach, we consider a sector-wise construction of the weight functions $w^B(\boldsymbol{x})$ and $w^Q(\boldsymbol{x})$. The process is outlined in Fig. 8. The 3-neighbourhood of the extraordinary vertex is partitioned into v sectors. Each sector consisting of 3×3 elements is parametrised with $\boldsymbol{\xi} = (\xi_1, \xi_2) \in \hat{\Omega} := [0, 1] \times [0, 1]$, see Fig. 8(a). The elements on the parametric domain $\hat{\Omega}$ are mapped using a mapping $\boldsymbol{\eta}(\boldsymbol{\xi})$ composed of a translation and a scaling to the reference element $\square$ for integration.

With the extraordinary vertex located at the origin $\boldsymbol{\xi} = (0, 0)$ of $\hat{\Omega}$, the implementation of the weight functions is identical on all the v sectors. Therefore, it is sufficient to detail the implementation only one of the sectors. As illustrated in Fig. 8(b), the weight function $w^Q(\boldsymbol{x})$ is constructed by first defining $w^Q(\boldsymbol{\xi})$ on the parametric domain $\hat{\Omega}$. We define $w^Q(\boldsymbol{\xi})$ as the tensor product of univariate weight functions $w^{\mathrm{I}}(\xi_1)$ and $w^{\mathrm{I}}(\xi_2)$,

$$w^Q(\boldsymbol{\xi}) = w^{\mathrm{I}}(\xi_1) \otimes w^{\mathrm{I}}(\xi_2). \tag{14}$$

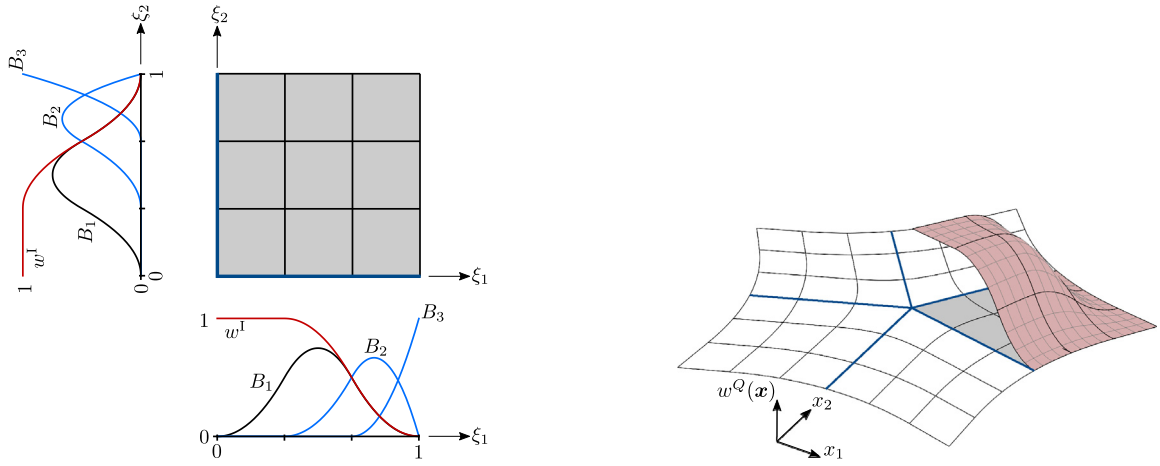

(a) Univariate weight functions and univariate B-splines

(b) $w^{Q}(\boldsymbol{x})$ for a given sector

Fig. 8. Construction of the weight function $w^{Q}(\boldsymbol{x})$ on one of the v sectors in the 3-neighbourhood of an extraordinary vertex. The weight function $w^{Q}(\boldsymbol{\xi})$ on the parametric domain $\hat{\Omega}$ is defined as the product of the univariate weight functions $w^{\mathrm{I}}(\xi_1)$ and $w^{\mathrm{I}}(\xi_2)$ in (a). Formally, $w^{Q}(\boldsymbol{x})$ on each element on the domain Ω in (b) is given by $w^{Q}(\boldsymbol{x}) = \boldsymbol{w}^{Q}(\boldsymbol{\xi}) \circ \boldsymbol{\eta}(\boldsymbol{\xi})^{-1} \circ \boldsymbol{x}(\boldsymbol{\eta})^{-1}$.

First, we assemble along the ξ_1 and ξ_2 axes the univariate weight functions for $w^{B}(\xi_1)$ and $w^{B}(\xi_2)$ by excluding the univariate B-splines which are not C^1 smooth at the origin $\boldsymbol{\xi} = (0,\, 0)$, see Fig. 8(a). Then, their complements to one yield

$$w^{\mathrm{I}}(\xi_i) = 1 - B_2(\xi_i) - B_3(\xi_i)\,, \quad i = 1,\, 2\,. \tag{15}$$

For evaluating the finite element integrals the weight function values at the quadrature points in the reference element $\square$ are required, which are obtained from

$$w^{Q}(\boldsymbol{\eta}) = w^{Q}(\boldsymbol{\xi}) \circ \boldsymbol{\eta}(\boldsymbol{\xi})^{-1}\,. \tag{16}$$

Here, the mapping $\eta(\boldsymbol{\xi})$ is, as mentioned above, composed of a translation and scaling and can be easily inverted.

4. Three-dimensional quadratic SB-splines

The proposed construction of SB-splines can also be extended to unstructured hexahedral meshes describing a domain $\Omega \subset \mathbb{R}^3$. A mesh consists of elements, i.e. hexahedral cells, their quadrilateral faces, edges and vertices. In 3D there are in addition to extraordinary vertices also extraordinary edges, see Fig. 1(c). Extraordinary edges are incident to two extraordinary vertices and regular edges to two regular vertices. In this paper, we assume that there are no edges with one ordinary and one extraordinary vertex and that all edges on the boundary of the domain are regular, i.e. are incident to two elements. Furthermore, the valence of an edge e is defined as the number of elements that share the same two vertices like the edge.

Well-designed hexahedral finite element meshes consist of a small number of chains of extraordinary edges. There are usually only a few extraordinary vertices with more than two incident extraordinary edges [17,20]. As in 2D, only the 3-neighbourhood of the extraordinary vertices and extraordinary edges is relevant for the proposed construction. In 3D, the union of the 3-neighbourhoods of all the extraordinary vertices in the mesh form a 6-element wide chain of elements as depicted in Fig. 9(a). We split the chain into several disjoint sets and refer to them as extraordinary prisms or extraordinary joints as illustrated in Figs. 9(b) and 9(c). Joints consist of the 3-neighbourhood of extraordinary vertices where more than two extraordinary edges meet. The remaining elements in the chain form the prisms. Each prism is connected to either a joint or the domain boundary.

In practice, the possible number of extraordinary edges meeting at an extraordinary vertex is limited. For the sake of clarity and conciseness, without loss of generality, we consider in this section only a joint with four incident prisms, i.e. $v = 4$, each of which has valence $e = 3$. The arbitrary v and e case can be similarly elaborated upon as is briefly discussed in Appendix D.

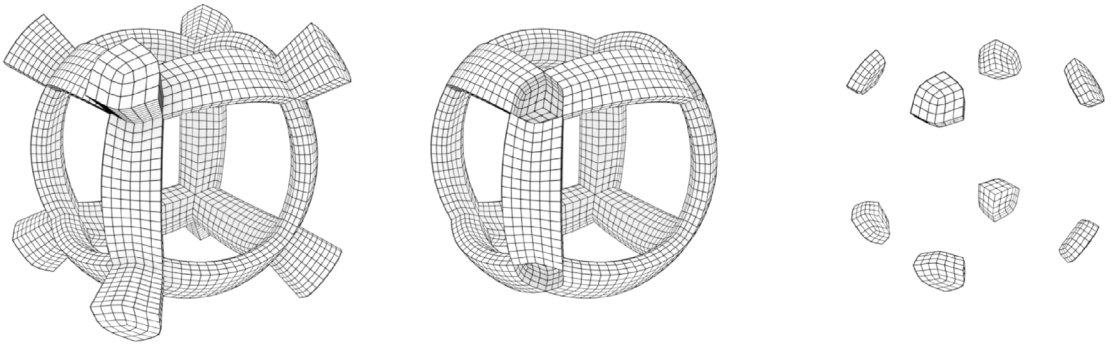

(a) 3-neighbourhood of extraordinary vertices **(b)** Extraordinary prisms **(c)** Extraordinary joints

Fig. 9. Extraordinary features in the unstructured hexahedral sphere mesh in Fig. 1. The 3-neighbourhood of the extraordinary vertices (a) are decomposed into twenty extraordinary prisms (b) and eight extraordinary joints (c). For illustration purposes, only twelve of the twenty extraordinary prisms are depicted in (b). The extraordinary vertices corresponding to the joints have $v = 4$ and the extraordinary edges corresponding to the prisms have $e = 3$.

4.1. Review of mixed B-splines

We now outline the extension of the mixed B-spline construction in Section 3.1 to an unstructured hexahedral mesh. The resulting tri-quadratic mixed B-splines are C^1 continuous away from the 1-neighbourhood of extraordinary edges and are only C^0 continuous along mesh faces incident to extraordinary vertices. Again, there is a one-to-one correspondence between the tri-quadratic mixed B-splines and the elements in the mesh (away from the boundaries) so that we assign a control vertex to each element. The support of the respective mixed B-spline consists of all elements sharing a vertex with the element.

As before, we first represent the non-zero mixed B-splines within an element with tri-quadratic Bézier basis functions. Subsequently, the corresponding Bézier control vertices are expressed as linear combinations of the mixed B-spline control vertices using the masks depicted in Fig. 10, the labelling of the vertices has been omitted for simplicity. The face Bézier control vertices are determined using the mask in Fig. 10(a), the edge Bézier control vertices using the mask in Fig. 10(b) and the corner Bézier control vertices using the mask in Fig. 10(c). The masks for edge and corner Bézier control vertices depend on the valence of the edge e and the valence of the vertex v, respectively. The centre Bézier control vertex has the same value as the element's respective mixed B-spline control vertex.

As in the two-dimensional case, combining the obtained Bézier basis control vertices with Bézier basis functions we can define a (local) parametrisation of the physical domain Ω as well as mixed B-splines. Recall that the parametrisation for the quadrilateral mesh in Section 3.1 was C^0 continuous across all edges incident to the extraordinary vertex. For hexahedral meshes the parametrisation is C^0 continuous across all faces incident to the extraordinary edge.

4.2. Construction of SB-splines

The construction of the blended C^1 smooth basis functions on unstructured hexahedral meshes follows the 1D and 2D constructions with only slight modification. The key idea is again to consider all the smooth mixed B-splines $B_i(\boldsymbol{x})$ to define the weight function $w^B(\boldsymbol{x})$ and its complement to one $w^Q(\boldsymbol{x}) = 1 - w^B(\boldsymbol{x})$. A naive implementation of this idea leads on hexahedral meshes to a single weight function $w^Q(\boldsymbol{x})$ with a support covering all the connected extraordinary prisms and joints in the mesh. Clearly, such a construction will lead to an overly dense stiffness matrix and adversely affect the approximation properties of the SB-splines. Therefore, as will be detailed in the following, the weight function $w^Q(\boldsymbol{x})$ is partitioned into two sets of locally supported weight functions $w^P_{k,\ell}(\boldsymbol{x})$ and $w^J_\ell(\boldsymbol{x})$ such that

$$w^Q(\boldsymbol{x}) = \sum_{k=1}^{n_P} \sum_{\ell=1}^{n_k} w^P_{k,\ell}(\boldsymbol{x}) + \sum_{\ell=1}^{n_J} w^J_\ell(\boldsymbol{x}) \,, \tag{17}$$

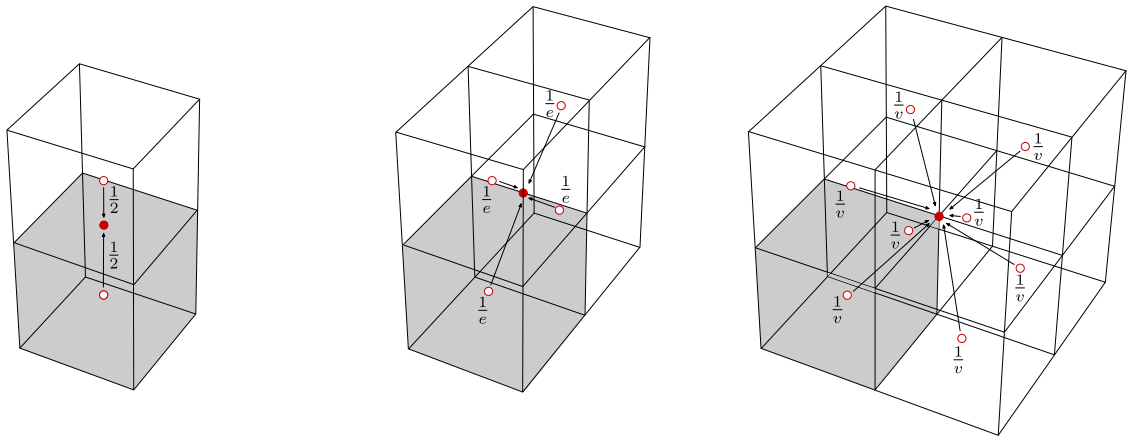

(a) Face mask **(b)** Edge mask for edge valence $e = 4$ **(c)** Corner mask for vertex valence $v = 8$

Fig. 10. Averaging masks for computing the tri-quadratic Bézier control vertices. The empty circles denote the mixed B-spline control vertices $\boldsymbol{x}_i$ and the solid circles the Bézier control vertices $\boldsymbol{c}_j$. The averaging masks for the edge Bézier control vertex in (b) and corner Bézier control vertex in (c) depend on the valence of the edge e and the valence of the vertex v, respectively.

where n_P is the number of extraordinary prisms, n_k is the number of weight functions defined along the extraordinary prism k and n_J is the number of extraordinary joints. In other words, there is one weight function for each extraordinary joint and several weight functions for each extraordinary prism. The construction of the prism weight functions $w^P_{k,\ell}(\boldsymbol{x})$ are introduced in Section 4.2.1 and the joint weight functions $w^J_\ell(\boldsymbol{x})$ in Section 4.2.2.

After the weight functions are determined, for blending we assign a tri-quadratic Bernstein basis $\boldsymbol{Q}(\boldsymbol{x})$ to each weight function. In the following, the domain of each tri-quadratic Bernstein basis $\boldsymbol{Q}(\boldsymbol{x})$ is assumed to be a cuboid enclosing the support of the corresponding weight function it is assigned to. We index the Bernstein basis similarly to the associated weight functions. Hence, analogous to 1D and 2D, the SB-splines are defined by

$$\boldsymbol{N}(\boldsymbol{x}) = \Big(w^B(\boldsymbol{x})\boldsymbol{B}(\boldsymbol{x})^\mathsf{T} \quad w^P_{1,1}(\boldsymbol{x})\boldsymbol{Q}_{1,1}(\boldsymbol{x})^\mathsf{T} \quad \cdots \quad w^P_{n_P,n_{n_P}}(\boldsymbol{x})\boldsymbol{Q}_{n_P,n_{n_P}}(\boldsymbol{x})^\mathsf{T} \quad w^J_1(\boldsymbol{x})\boldsymbol{Q}_1(\boldsymbol{x})^\mathsf{T} \quad \cdots \quad w^J_{n_J}(\boldsymbol{x})\boldsymbol{Q}_{n_J}(\boldsymbol{x})^\mathsf{T} \Big)^\mathsf{T} . \tag{18}$$

4.2.1. *Weight functions for extraordinary prisms*

The weight functions for one extraordinary prism are obtained as illustrated in Figs. 11 and 12. The two ends of the prism are either incident to an extraordinary joint or the boundary of the domain Ω. The centre of the prism consists of n_{ee} extraordinary edges of valence $e = 3$. For constructing the weight functions the prism is partitioned into e sectors, see Fig. 11(a). Each sector consists of $3 \times 3 \times n_{ee}$ elements and is parametrised using $\boldsymbol{\xi} = (\xi_1, \xi_2, \xi_3) \in \hat{\Omega}$ with the parametric domain $\hat{\Omega} := [0, 1] \times [0, 1] \times [0, 1]$. The extraordinary edges are located along the parametric axis $\boldsymbol{\xi} = (0, 0, \xi_3)$. The elements on $\hat{\Omega}$ are mapped to the reference element $\square$ for integration using a mapping $\boldsymbol{\eta}(\boldsymbol{\xi})$ composed of a translation, rotation and scaling.

On a given sector of the k-th prism, we define n_k univariate weight functions $w^{\mathrm{II}}_{k,\ell}(\xi_3)$ from the available quadratic univariate B-splines $B_i(\xi_3)$. The number of weight functions n_k can be chosen flexibly, as long as

- each $w^{\mathrm{II}}_{k,\ell}(\xi_3)$ is the sum of a certain number of consecutive B-splines,
- each $w^{\mathrm{II}}_{k,\ell}(\xi_3)$ has vanishing derivatives at the endpoints of its support,
- each B-spline is used to build exactly one $w^{\mathrm{II}}_{k,\ell}(\xi_3)$, cf. Fig. 11(b),
- and the sum of all $w^{\mathrm{II}}_{k,\ell}(\xi_3)$ is equal to 1.

For instance, in Fig. 11(b) the univariate weight functions $w^{\mathrm{II}}_{k,\ell}(\xi_3)$ are defined as

$$w^{\mathrm{II}}_{k,1}(\xi_3) = \sum_{i=1}^{4} B_i(\xi_3) , \quad w^{\mathrm{II}}_{k,2}(\xi_3) = \sum_{i=5}^{8} B_i(\xi_3) , \quad w^{\mathrm{II}}_{k,3}(\xi_3) = \sum_{i=9}^{12} B_i(\xi_3) . \tag{19}$$

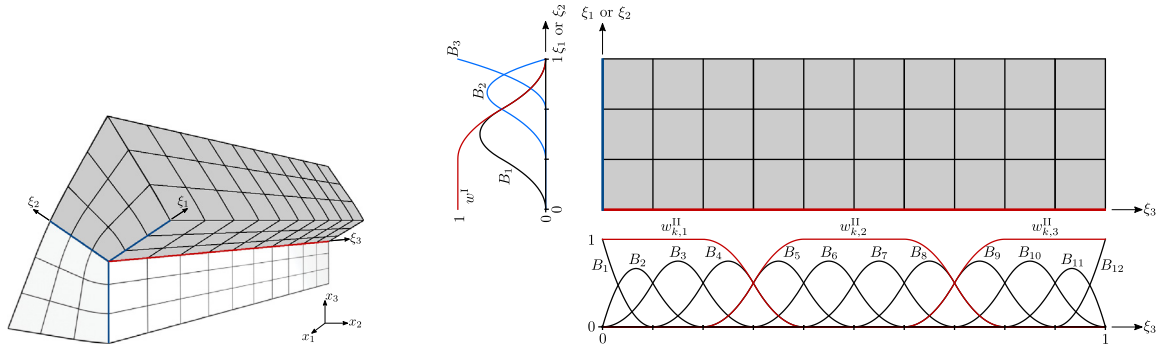

(a) Extraordinary prisms (2 sectors shown) **(b)** Univariate weight functions and B-splines

Fig. 11. Construction of the weight functions for an extraordinary prism. The two ends of the prism are either incident to an extraordinary joint or the boundary of the domain Ω. In (a) only two of the e sectors are shown for visualisation purposes. Each sector consists of $3\times3\times n_{ee}$ elements and has a corresponding (cuboidal) parametric domain $\hat{\Omega}$ as illustrated in (b). The weight functions $w^P_{k,\ell}(\boldsymbol{\xi})$ for one of the e sectors are defined as the tensor product of the bivariate weight function $w^{\mathrm{I}}(\xi_1)\otimes w^{\mathrm{II}}(\xi_2)$ and the three univariate weight functions $w^{\mathrm{II}}_{k,1}(\xi_3)$, $w^{\mathrm{II}}_{k,2}(\xi_3)$ and $w^{\mathrm{II}}_{k,3}(\xi_3)$.

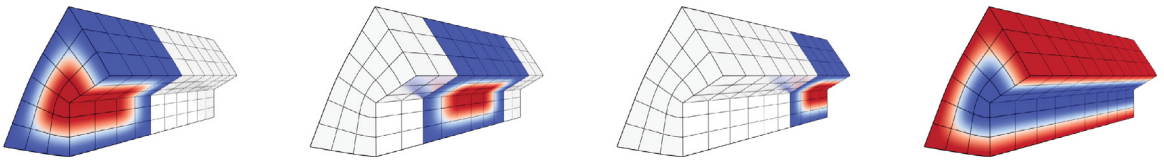

(a) $w^P_{k,1}(\boldsymbol{x})$ **(b)** $w^P_{k,2}(\boldsymbol{x})$ **(c)** $w^P_{k,3}(\boldsymbol{x})$ **(d)** $w^B(\boldsymbol{x})$

Fig. 12. Weight functions for the extraordinary prism. The weight functions $w^P_{k,1}(\boldsymbol{x})$, $w^P_{k,2}(\boldsymbol{x})$ and $w^P_{k,3}(\boldsymbol{x})$ are obtained by choosing three univariate weight functions $w^{\mathrm{II}}_{k,1}(\xi_3)$, $w^{\mathrm{II}}_{k,2}(\xi_3)$ and $w^{\mathrm{II}}_{k,3}(\xi_3)$ along the centre of the extraordinary prism as depicted in Fig. 11(b). The weight function $w^B(\boldsymbol{x})$ is their complement to one, i.e. $w^B(\boldsymbol{x}) = 1 - w^P_{k,1}(\boldsymbol{x}) - w^P_{k,2}(\boldsymbol{x}) - w^P_{k,3}(\boldsymbol{x})$. The scalar field ranges between 0 (blue) and 1 (red). (For interpretation of the references to colour in this figure legend, the reader is referred to the web version of this article.)

The isocontours of the three weight functions and their complement to one $w^B(\boldsymbol{x})$ on two of the three sectors are depicted in Fig. 12. Note that choosing a large n_k ensures that the SB-splines have small support sizes.

Following the above, the trivariate weight functions $w^P_{k,\ell}(\xi_1,\xi_2,\xi_3)$ are defined as the tensor product of the bivariate weight function $w^{\mathrm{I}}(\xi_1)\otimes w^{\mathrm{I}}(\xi_2)$, introduced in Section 3.2, and the n_k univariate weight functions $w^{\mathrm{II}}_{k,\ell}(\xi_3)$,

$$w^P_{k,\ell}(\boldsymbol{\xi}) = w^{\mathrm{I}}(\xi_1)\otimes w^{\mathrm{I}}(\xi_2)\otimes w^{\mathrm{II}}_{k,\ell}(\xi_3)\,, \quad \ell = 1,\ldots,n_k\,. \tag{20}$$

The construction is repeated for all prisms to obtain weight functions for all k.

4.2.2. Weight functions for extraordinary joints

Without loss of generality, we consider a single extraordinary joint with valence $v = 4$ shared by four extraordinary prisms each of which has valence $e = 3$, see Fig. 9, and describe the construction of its associated weight function. To simplify the construction of the extraordinary joint weight function $w^J_\ell(\boldsymbol{x})$ we require that the support of the already defined prism weight functions $w^P_{k,\ell}(\boldsymbol{x})$ do not overlap at the joint. Recall from Figs. 11 and 12 that the support of the prism weight functions $w^P_{k,\ell}(\boldsymbol{x})$ corresponds in the $\xi_1\xi_2$-plane to the 3-neighbourhood of the extraordinary vertex. Hence, we choose the 3-neighbourhood of the extraordinary vertex at the centre of the joint for constructing the weight function $w^J_\ell(\boldsymbol{x})$ as illustrated in Fig. 13(a). At the boundary of the 3-neighbourhood, the joint meets different prisms. The intersection of the joint with each prism is composed of $3\times3\times e$ quadrilateral faces, with e the valence of the prism's extraordinary edge. We require across each of the $3\times3\times e$ faces that the value and derivatives of the weight function $w^J_\ell(\boldsymbol{x})$ match those of the unique non-zero prism weight function. For

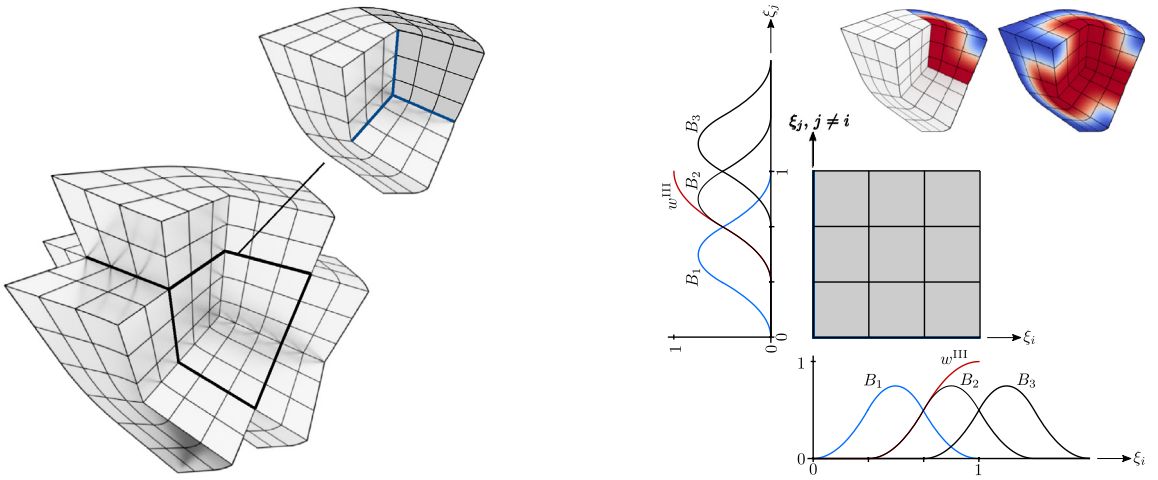

(a) Extraordinary joint and attached prisms

(b) Univariate weight functions and B-splines

Fig. 13. Construction of the extraordinary joint weight function $w^J_\ell(\boldsymbol{x})$ on one of the $v = 4$ sectors. Each sector consists of the $3 \times 3 \times 3$ elements shown in (a). The weight function $w^J_\ell(\boldsymbol{\xi})$ is obtained using the univariate weight functions $w^{\mathrm{III}}(\xi_1)$, $w^{\mathrm{III}}(\xi_2)$ and $w^{\mathrm{III}}(\xi_3)$ shown in (b) which are simply the complement to one of $w^{\mathrm{I}}(\xi_i) = 1 - w^{\mathrm{III}}(\xi_i)$ with $i = 1, 2, 3$ shown earlier in Fig. 11(b). The result is depicted at the top right of (b) with the scalar field ranging between 0 (blue) and 1 (red). (For interpretation of the references to colour in this figure legend, the reader is referred to the web version of this article.)

instance, in the already discussed example in Fig. 11(b) the weight functions $w^P_{k,1}(\boldsymbol{x})$ and $w^P_{k,3}(\boldsymbol{x})$ corresponding to $w^{\mathrm{II}}_{k,1}(\xi_3)$ and $w^{\mathrm{II}}_{k,3}(\xi_3)$ have to smoothly connect to the respective joint weight functions.

To construct the joint weight function $w^J_\ell(\boldsymbol{x})$ we follow once more a sector-wise approach as outlined in Fig. 13. The joint is partitioned into $v = 4$ sectors each consisting of $3 \times 3 \times 3$ elements. Each sector is parametrised using $\boldsymbol{\xi} = (\xi_1, \xi_2, \xi_3) \in \hat{\Omega}$ on the parametric domain $\hat{\Omega} := [0, 1] \times [0, 1] \times [0, 1]$. The extraordinary edges of the attached four prisms meet at the origin $\boldsymbol{\xi} = (0, 0, 0)$ of the domain $\hat{\Omega}$. We define the joint weight function $w^J_\ell(\boldsymbol{\xi})$ as

$$\begin{aligned} w^J_\ell(\boldsymbol{\xi}) = 1 &- w^{\mathrm{III}}(\xi_1) \otimes w^{\mathrm{III}}(\xi_2) \otimes w^{\mathrm{III}}(\xi_3) - \big(1 - w^{\mathrm{III}}(\xi_1)\big) \otimes w^{\mathrm{III}}(\xi_2) \otimes w^{\mathrm{III}}(\xi_3) \\ &- w^{\mathrm{III}}(\xi_1) \otimes \big(1 - w^{\mathrm{III}}(\xi_2)\big) \otimes w^{\mathrm{III}}(\xi_3) - w^{\mathrm{III}}(\xi_1) \otimes w^{\mathrm{III}}(\xi_2) \otimes \big(1 - w^{\mathrm{III}}(\xi_3)\big) \,, \end{aligned} \tag{21}$$

where the univariate weight functions $w^{\mathrm{III}}(\xi_i)$ are, as depicted in Fig. 13(b), assembled from the smooth quadratic B-splines defined along the ξ_1, ξ_2 or ξ_3 axes. That is,

$$w^{\mathrm{III}}(\xi_i) = B_2(\xi_i) + B_3(\xi_i) \quad i = 1,\ 2,\ 3\,. \tag{22}$$

In Fig. 14 the isocontours of the obtained joint weight function $w^J_\ell(\boldsymbol{x})$, the weight functions $w^P_{k,\ell}(\boldsymbol{x})$ of the attached four prisms and their complement to one $w^B(\boldsymbol{x})$ are shown. In Appendix D we briefly demonstrate that the joint and prism weight functions for arbitrary vertex and edge valences v and e can be constructed following same approach.

5. Examples

We proceed to establish the finite element convergence properties and accuracy of the SB-splines in solving Poisson and biharmonic problems. The respective weak forms and the details of the finite element discretisation are summarised in Appendix B. In all the examples we use sufficiently smooth manufactured solutions and focus on quadratic basis functions, except in 1D where we also consider cubic basis functions. As known from the isogeometric analysis literature the optimal convergence rates for the Poisson problem discretised with standard quadratic B-splines are 3 in the L^2 norm and 2 in the H^1 seminorm [68]. In contrast, the optimal convergence rates for the biharmonic problem discretised with quadratic B-splines are 2 in the L^2 norm and the H^1 seminorm and 1 in the H^2 seminorm [69].

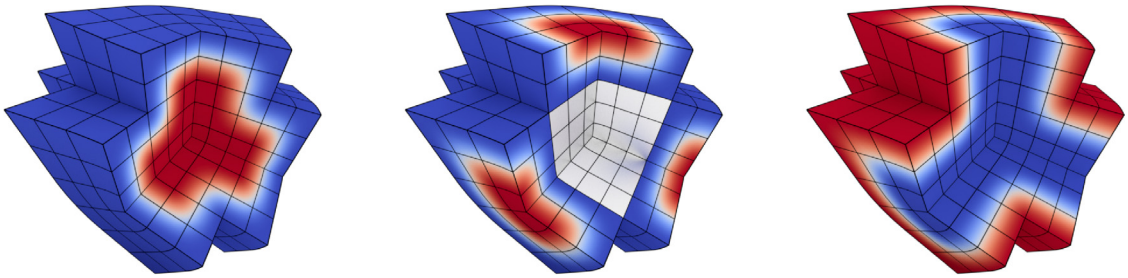

(a) $w^J_\ell(\boldsymbol{x})$ **(b)** $w^P_{k,\ell}(\boldsymbol{x})$ **(c)** $w^B(\boldsymbol{x})$

Fig. 14. Extraordinary joint weight function $w^J_\ell(\boldsymbol{x})$, extraordinary prism weight functions $w^P_{k,\ell}(\boldsymbol{x})$ and their complement to one $w^B(\boldsymbol{x})$. The scalar field ranges between 0 (blue) and 1 (red). (For interpretation of the references to colour in this figure legend, the reader is referred to the web version of this article.)

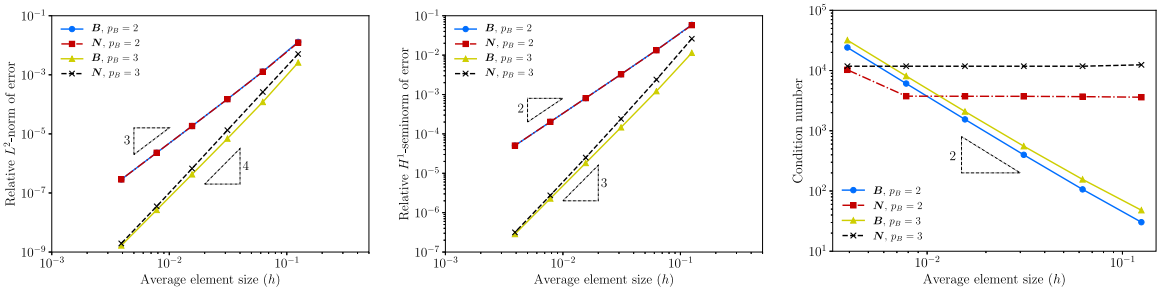

(a) Relative L^2-norm of error **(b)** Relative H^1-seminorm of error **(c)** Condition number

Fig. 15. One-dimensional Poisson–Dirichlet problem. Finite element convergence and condition number of the stiffness matrices for the C^1 continuous SB-splines $\boldsymbol{N}(x)$ and the mixed smoothness B-splines $\boldsymbol{B}(x)$, consisting of C^0 and C^{p_B-1} continuous basis functions.

5.1. One-dimensional Poisson problem

As a first example we consider the solution of a one-dimensional Poisson–Dirichlet problem $-\mathrm{d}^2u/\mathrm{d}x^2 = f$ on the domain $\Omega = (0, 1)$. The body force $f(x)$ is chosen such that the solution is

$$u(x) = \sin(3\pi x) \ . \tag{23}$$

The domain is parametrised using non-uniform B-splines of degree $p_B = 2$ and $p_B = 3$ in turn. The knot vector and control points x_i are selected so that each element has the same size h. We intentionally introduce a C^0 continuous kink at the midspan $x = 1/2$ by setting the knot multiplicity to p_B therein. In addition, we use an open knot vector which allows the Dirichlet boundary condition to be imposed strongly.

In the following we compare the finite element convergence and the condition number of the stiffness matrices for the SB-splines $\boldsymbol{N}(x)$ with the ones for the mixed B-splines $\boldsymbol{B}(x)$, consisting of C^0 and C^{p_B-1} continuous basis functions. The C^1 continuous SB-splines $\boldsymbol{N}(x)$ are constructed by blending B-splines $\boldsymbol{B}(x)$ with Bernstein basis $\boldsymbol{Q}(x)$ of same polynomial degree $p_Q = p_B$. In comparison to B-splines $\boldsymbol{B}(x)$ the SB-splines $\boldsymbol{N}(x)$ have the additional degrees of freedom $n_Q = p_Q + 1$. We begin with an initial coarse mesh of $n_e = 8$ elements and obtain finer meshes using knot insertion. Figs. 15(a) and 15(b) show that the SB-splines $\boldsymbol{N}(x)$ yield optimal convergence rates for both polynomial degrees $p_B = 2$ and $p_B = 3$. In addition, the approximation error remains in the same order of magnitude with or without blending. The condition number of the respective stiffness matrices is plotted in Fig. 15(c). When the mesh size h is relatively large the SB-splines lead to significantly larger condition numbers than the B-splines. Interestingly, the condition numbers for SB-splines are almost independent of mesh size. Overall, the SB-splines condition numbers compare favourably with the B-splines condition numbers.

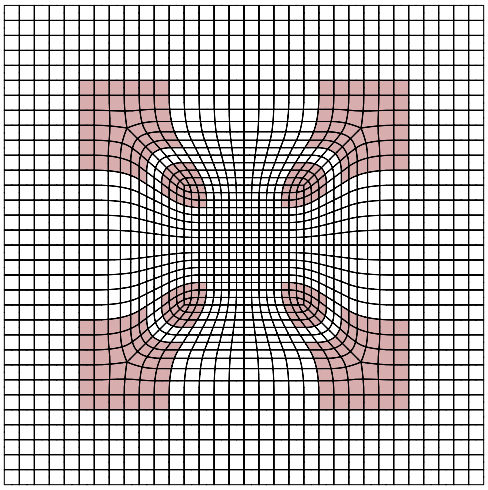

Fig. 16. Initial semi-structured coarse mesh of the square domain. The 32 elements in the eight blending domains are shown shaded.

5.2. Poisson and biharmonic problems on a square domain

We consider next the Poisson–Dirichlet and biharmonic problems on a square domain $\Omega = (0, 1) \times (0, 1)$. Fig. 16 shows the initial semi-structured coarse mesh with 8 extraordinary vertices. The boundary of the square domain is parametrised using open, uniform bi-quadratic B-splines. For the Poisson–Dirichlet problem, the Dirichlet boundary condition is imposed using Nitsche's method with the stabilisation parameter chosen as $\gamma = 10/h^2$, see Appendix B. For the biharmonic problem, we use the penalty approach with the stabilisation parameter chosen as $\gamma = 1/h^2$. In comparison to mixed B-splines $\boldsymbol{B}(\boldsymbol{x})$, for the SB-splines $\boldsymbol{N}(\boldsymbol{x})$ the additional degrees of freedom are $n_Q = 8 \times 9 = 72$. We refine the mesh using a refinement scheme described in Appendix C, so that the number of extraordinary vertices remains constant and the blending domains become increasingly smaller. In all meshes there are 8 extraordinary vertices and in total 32 elements in the respective blending domains.

We approximate the finite element integrals using the Gauss–Legendre quadrature rule. In order to examine the effect of the number of quadrature points n_{gp} on the finite element convergence, for the SB-splines $\boldsymbol{N}(\boldsymbol{x})$, we vary n_{gp} for the domain integrals and use always 3 quadrature points for the boundary integrals. For the mixed B-splines $\boldsymbol{B}(\boldsymbol{x})$, we use for the domain integrals and boundary integrals 3×3 and 3 quadrature points, respectively.

For the two-dimensional Poisson–Dirichlet problem, the body force $f(\boldsymbol{x})$ is chosen so that the solution is equal to

$$u(\boldsymbol{x}) = \sin(6x_1)\sin(8x_2)\ . \tag{24}$$

Fig. 17 confirms that the SB-splines are optimally convergent provided that at least $n_{gp} = 3 \times 3$ quadrature points are used. For $n_{gp} = 3 \times 3$, as the mesh is refined the approximation error remains in the same order of magnitude with or without blending. We conjecture that the number of quadrature points n_{gp} for the SB-splines $\boldsymbol{N}(\boldsymbol{x})$ to achieve the optimal convergence rate is relatively small because the weight functions $w^B(\boldsymbol{x})$ and $w^Q(\boldsymbol{x})$ are assembled from smooth piecewise quadratic B-splines.

For the two-dimensional biharmonic problem, the body force $f(\boldsymbol{x})$ is chosen so that the solution is equal to

$$u(\boldsymbol{x}) = \frac{\sin(\pi x_1)\sin(\pi x_2)}{4\pi^4}\ . \tag{25}$$

As the mixed B-splines $\boldsymbol{B}(\boldsymbol{x})$ are not globally C^1 continuous on the considered semi-structured quadrilateral mesh, we examine only the finite element convergence using the C^1 continuous SB-splines $\boldsymbol{N}(\boldsymbol{x})$. Fig. 18 shows that the SB-splines $\boldsymbol{N}(\boldsymbol{x})$ are optimally convergent for the biharmonic problem provided that a minimum of $n_{gp} = 2 \times 2$ is used for the quadrature. However, note that the relative H^2-seminorm of error improves when $n_{gp} = 3 \times 3$ is used.

In addition to the convergence rate, we examine the finite element solution $u^h(\boldsymbol{x})$ for the biharmonic problem qualitatively. Fig. 19 shows the finite element solution $u^h(\boldsymbol{x})$ and its first and second partial derivatives with respect

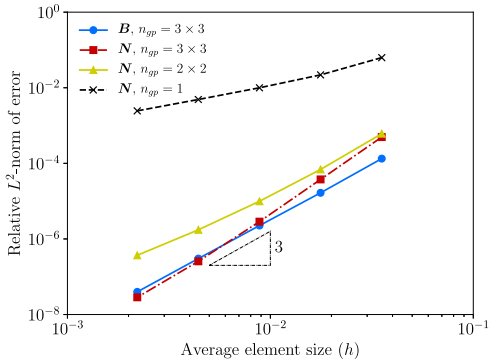

(a) Relative L^2-norm of error

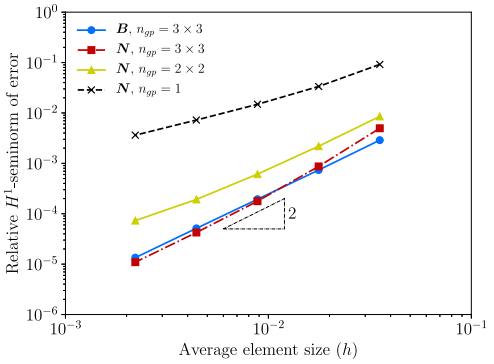

(b) Relative H^1-seminorm of error

Fig. 17. Poisson–Dirichlet problem on a square domain. Convergence of the mixed B-spline $\boldsymbol{B}(\boldsymbol{x})$ and SB-spline $\boldsymbol{N}(\boldsymbol{x})$ solutions.

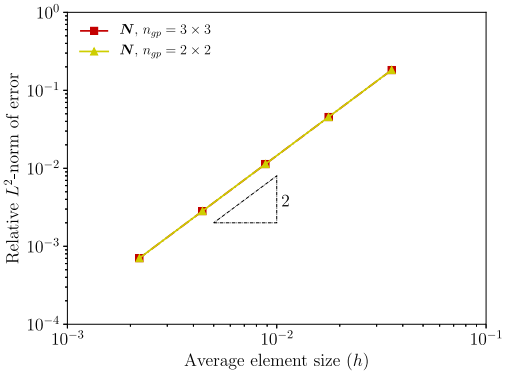

(a) Relative L^2-norm of error

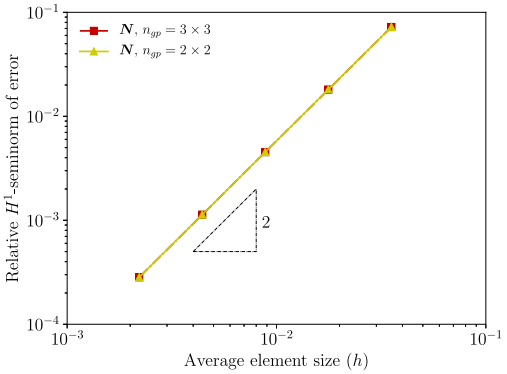

(b) Relative H^1-seminorm of error

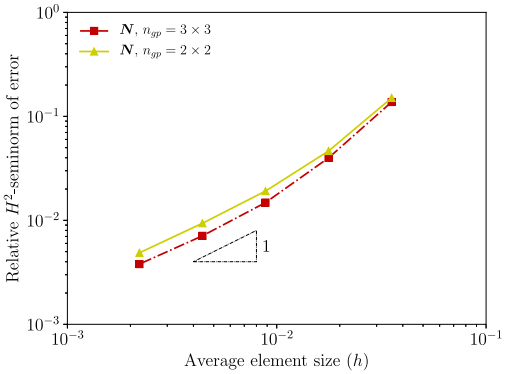

(c) Relative H^2-seminorm of error

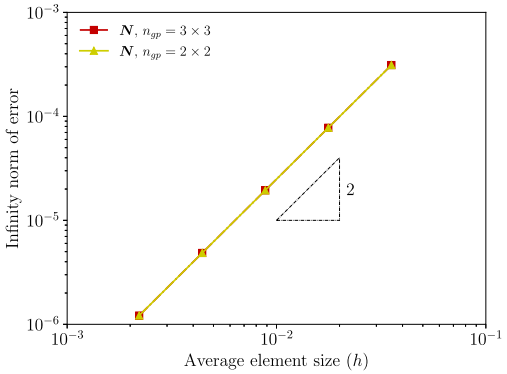

(d) L^∞-norm of error

Fig. 18. Biharmonic problem on a square domain. Convergence with SB-splines $\boldsymbol{N}(\boldsymbol{x})$.

to x_1 for the initial coarse mesh. Since the SB-splines $\boldsymbol{N}(\boldsymbol{x})$ are globally C^1 continuous, both the finite element solution $u^h(\boldsymbol{x})$ and its first partial derivative with respect to x_1 are continuous as visible in Figs. 19(a) and 19(b), respectively. Furthermore, as known the spatial derivatives of $u^h(\boldsymbol{x})$ often exhibit short-wavelength oscillations near the extraordinary vertices. Similarly, we observe such oscillations specifically for the second spatial derivatives in

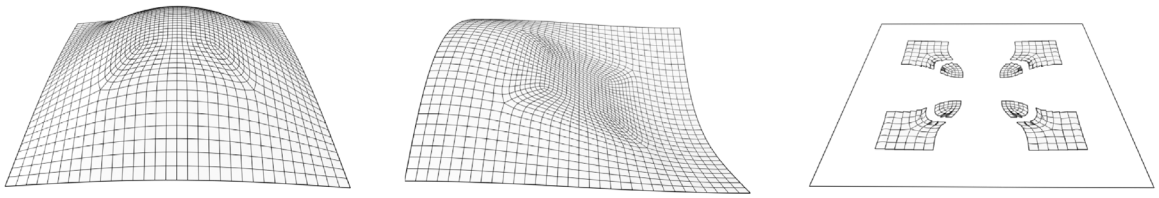

(a) u^h, out-of-plane scale factor: 100 **(b)** $\frac{\partial u^h}{\partial x_1}$, out-of-plane scale factor: 25 **(c)** $\frac{\partial^2 u^h}{\partial x_1^2}$, out-of-plane scale factor: 2

Fig. 19. Biharmonic problem on a square domain. The finite element solution u^h and its first and second partial derivatives with respect to x_1 for the initial coarse mesh. All plots have been warped in the out-of-plane direction using the stated scale factors. In (a) and (b) all elements are shown whereas in (c) only elements in the blending domain Ω_Q are shown.

the blending domain Ω_Q as depicted in Fig. 19(c). However, there are no oscillations in the 1-neighbourhood of the extraordinary vertices.

5.3. Biharmonic problem on v-gon domains

In some smooth basis function construction techniques, the respective finite element convergence rates are known to deteriorate when the valence v is increased, see the discussion in [29]. Therefore, we investigate next the convergence rate of the SB-splines $\boldsymbol{N}(\boldsymbol{x})$ for different valences. To this end, we consider the biharmonic problem on the five v-gon domains with $v \in \{3, 5, 6, 7, 8\}$ shown in Fig. 20. For each domain, the extraordinary vertex is located at the origin $\boldsymbol{x} = (0,\ 0)$. The boundary is parametrised with open, uniform bi-quadratic B-splines. To impose the boundary conditions, we use the penalty approach with the stabilisation parameter chosen as $\gamma = 1000/h^2$. As shown to be sufficient for the biharmonic problem in Section 5.2, we use 3×3 and 3 quadrature points for approximating the domain and boundary integrals, respectively. Similarly, we refine the mesh using the refinement scheme described in Appendix C. The body force $f(\boldsymbol{x})$ is chosen such that the solution is equal to

$$u(\boldsymbol{x}) = \sin(3x_1)\cos(3x_2)\ . \tag{26}$$

Fig. 21 shows the finite element convergence using the SB-splines $\boldsymbol{N}(\boldsymbol{x})$. Although the convergence rates for the first few coarse meshes are slightly fluctuating, overall the SB-splines $\boldsymbol{N}(\boldsymbol{x})$ are optimally convergent. In other words, the convergence rate is identical for the considered valences $v \in \{3, 5, 6, 7, 8\}$. The increase of the valence leads, however, to a small increase in the convergence constants. This finding suggests that the SB-splines $\boldsymbol{N}(\boldsymbol{x})$ are robust since the studied valences $v \in \{3, 5, 6, 7, 8\}$ are the most prevalent in well-designed meshes.

5.4. Poisson and biharmonic problems on a spherical domain

As a final example, we consider the Poisson–Dirichlet and biharmonic problems on the spherical domain in Fig. 1. The spherical domain has a radius of 2.55 and is centred at the global origin $\boldsymbol{x} = (0, 0, 0)$. As an approximation to the spherical domain, the parametrised hexahedral mesh in Fig. 1(b) has an average mesh size $h = 0.4228$ and consists of 20 extraordinary prisms of valence $e = 3$ and 8 extraordinary joints. The boundary of the spherical domain is parametrised using open, uniform tri-quadratic B-splines. For the Poisson–Dirichlet problem, the Dirichlet boundary condition is imposed using Nitsche's method with the stabilisation parameter chosen as $\gamma = 10/h^2$. For the biharmonic problem, we use the penalty approach with the stabilisation parameter chosen as $\gamma = 1000/h^2$. The numbers of degrees of freedom for the mixed B-splines $\boldsymbol{B}(\boldsymbol{x})$ and the SB-splines $\boldsymbol{N}(\boldsymbol{x})$ are 6413 and $6413 + (20 + 8) \times 27 = 7169$, respectively.

For the three-dimensional Poisson–Dirichlet problem, the body force $f(\boldsymbol{x})$ is chosen so that the solution is equal to

$$u(\boldsymbol{x}) = \sin\left(\frac{x_1}{2}\right)\sin\left(\frac{x_2}{2}\right)\sin\left(\frac{x_3}{4}\right)\ . \tag{27}$$

We compare numerically the finite element solution $u^h(\boldsymbol{x})$ between $\boldsymbol{B}(\boldsymbol{x})$ and $\boldsymbol{N}(\boldsymbol{x})$. The relative L^2-norms of error for $\boldsymbol{B}(\boldsymbol{x})$ and $\boldsymbol{N}(\boldsymbol{x})$ are 4.9111×10^{-4} and 3.9034×10^{-4}, respectively, whereas the relative H^1-seminorms of error

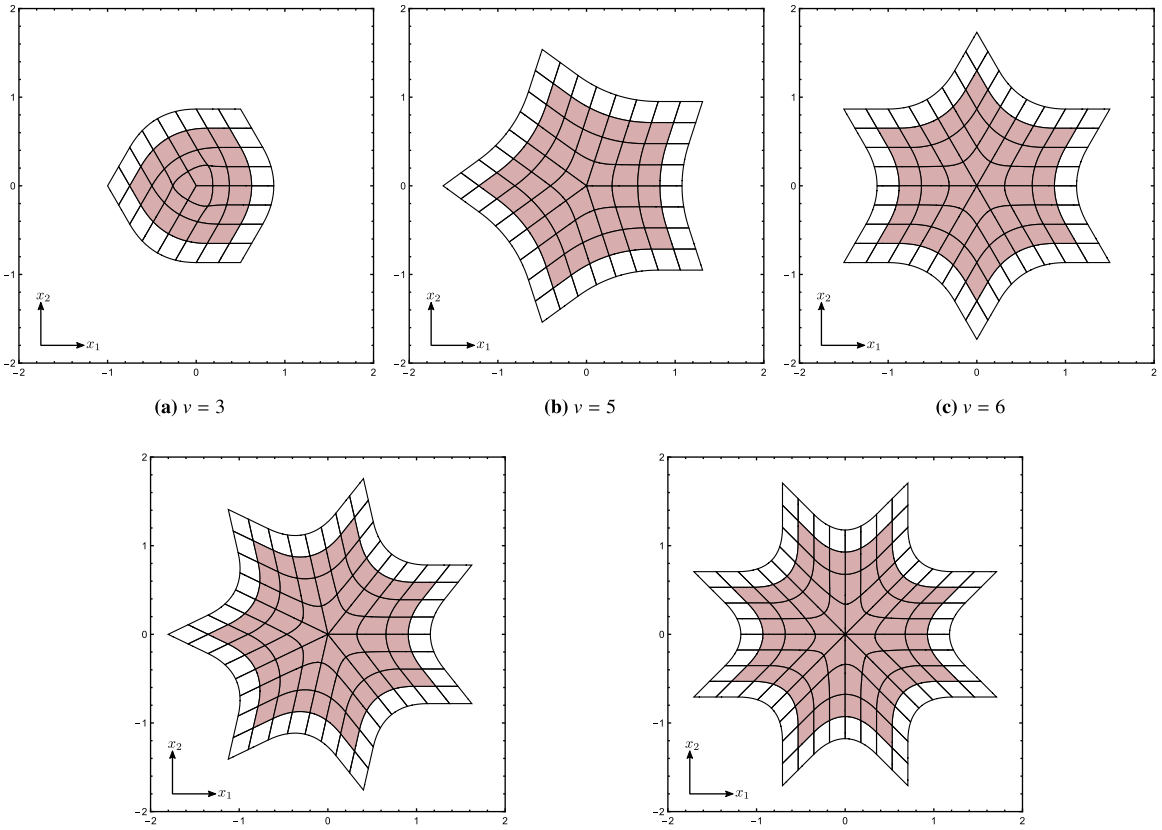

(a) $v = 3$ **(b)** $v = 5$ **(c)** $v = 6$

(d) $v = 7$ **(e)** $v = 8$

Fig. 20. Initial coarse meshes for the v-gon domains. For each initial coarse mesh the blending domain Ω_Q is shaded in pink. (For interpretation of the references to colour in this figure legend, the reader is referred to the web version of this article.)

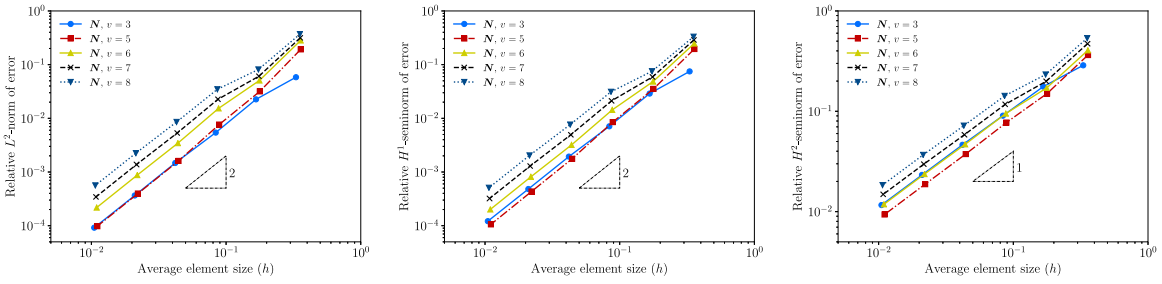

(a) Relative L^2-norm of error **(b)** Relative H^1-seminorm of error **(c)** Relative H^2-seminorm of error

Fig. 21. Biharmonic problem on v-gon domains. Convergence with SB-splines $\boldsymbol{N}(\boldsymbol{x})$.

for $\boldsymbol{B}(\boldsymbol{x})$ and $\boldsymbol{N}(\boldsymbol{x})$ are $5.1337 \times \times 10^{-3}$ and 3.5630×10^{-3}, respectively. Therefore, the approximation error has the same order of magnitude with and without blending. Fig. 22 illustrates the first partial derivative of the finite element solution with respect to x_1. As can be seen, both $\boldsymbol{B}(\boldsymbol{x})$ and $\boldsymbol{N}(\boldsymbol{x})$ yield an accurate approximation to the first partial derivative of the analytical solution with respect to x_1. In addition, Fig. 23 ascertains that the SB-splines $\boldsymbol{N}(\boldsymbol{x})$ are globally C^1 continuous. For instance, the mixed B-splines $\boldsymbol{B}(\boldsymbol{x})$ yield C^0 continuous finite element solution $u^h(\boldsymbol{x})$ near the extraordinary edges as inferred from the discontinuity of the first partial derivative of u^h with respect to x_1

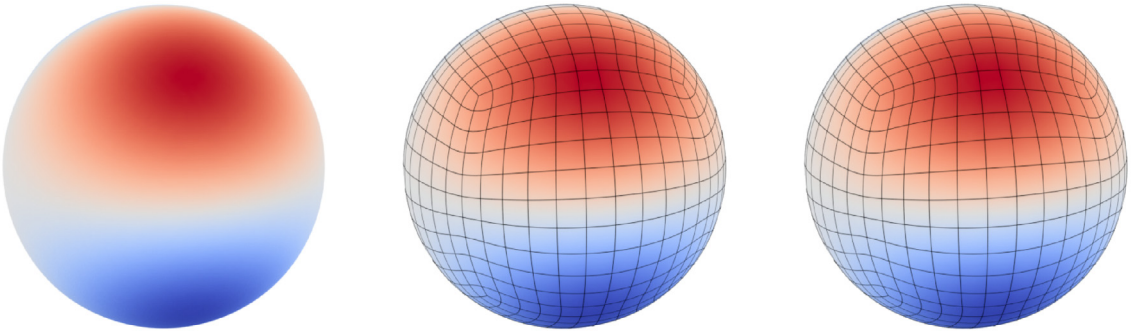

(a) Analytical $\frac{\partial u(\boldsymbol{x})}{\partial x_1}$ **(b)** $\frac{\partial u^h(\boldsymbol{x})}{\partial x_1}$ using $\boldsymbol{B}(\boldsymbol{x})$ **(c)** $\frac{\partial u^h(\boldsymbol{x})}{\partial x_1}$ using $\boldsymbol{N}(\boldsymbol{x})$

Fig. 22. Poisson–Dirichlet problem on a spherical domain. Isocontours of the first partial derivative of the finite element solution with respect to x_1 on the spline surface. The scalar field ranges between -0.18 (blue) and 0.18 (red). (For interpretation of the references to colour in this figure legend, the reader is referred to the web version of this article.)

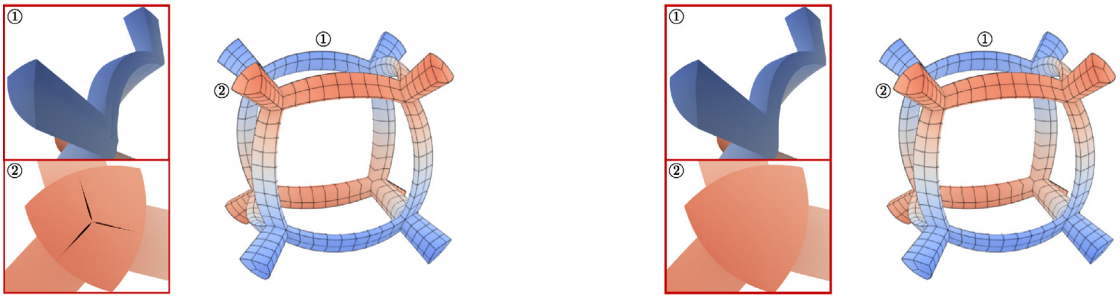

(a) $\frac{\partial u^h(\boldsymbol{x})}{\partial x_1}$ using $\boldsymbol{B}(\boldsymbol{x})$ **(b)** $\frac{\partial u^h(\boldsymbol{x})}{\partial x_1}$ using $\boldsymbol{N}(\boldsymbol{x})$

Fig. 23. Poisson–Dirichlet problem on a spherical domain. Isocontours of the first partial derivative of the finite element solution with respect to x_1 near the extraordinary edges. For consistency, the scalar field herein has the same scale as Fig. 22.

in Fig. 23(a). In contrast, the first partial derivative of u^h with respect to x_1 using $\boldsymbol{N}(\boldsymbol{x})$ is continuous in the same subdomains as shown in Fig. 23(b).

For the three-dimensional biharmonic problem, the body force $f(\boldsymbol{x})$ is chosen so that the solution is equal to

$$u(\boldsymbol{x}) = \frac{1}{8\pi} \sin\left(\frac{\pi x_1}{8}\right) \sin\left(\frac{\pi x_2}{8}\right) \sin\left(\frac{\pi x_3}{8}\right) . \tag{28}$$

Using the SB-splines $\boldsymbol{N}(\boldsymbol{x})$, the relative L^2-norm of error, relative H^1-seminorm of error and relative H^2-seminorm of error are 9.8943×10^{-4}, 3.7825×10^{-3} and 6.4669×10^{-2}, respectively. Fig. 24 shows that the SB-splines $\boldsymbol{N}(\boldsymbol{x})$ yield a satisfactory finite element approximation to the analytical solution.

6. Conclusions

We introduced the SB-splines, i.e. a smooth blended B-spline construction, for semi-structured quadrilateral and hexahedral meshes and demonstrated their optimal convergence in the case of quadratic basis function. We assemble the smooth weight functions required for blending from the smooth mixed B-splines defined on the regular regions of the unstructured mesh. The weight functions multiplied with the available mixed B-splines and additionally introduced Bernstein basis functions yield the new basis functions. As shown numerically, the SB-splines can be efficiently integrated using standard Gauss–Legendre quadrature with a very small number of quadrature points. In the blending region, the new basis functions have slightly larger support close to the extraordinary features. For instance, in 2D the support consists of the 3-neighbourhood of the extraordinary vertex. Remarkably, the numerically

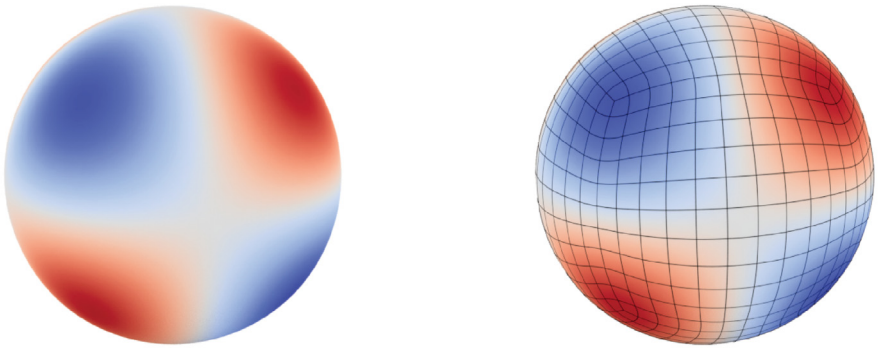

(a) Analytical $u(\boldsymbol{x})$ **(b)** $u^h(\boldsymbol{x})$ using $\boldsymbol{N}(\boldsymbol{x})$

Fig. 24. Biharmonic problem on a spherical domain. Isocontours of the finite element solution on the spline surface. The scalar field ranges between -0.43 (blue) and 0.43 (red). (For interpretation of the references to colour in this figure legend, the reader is referred to the web version of this article.)

determined convergence rates in 2D are optimal for both Poisson and biharmonic problems and are independent of the valence of the extraordinary vertex. However, the convergence constants show a slight increase with an increase in valence, which may be explained by the short-wavelength oscillations, or ripples, in the higher-order derivatives at the blending region. As discussed, on unstructured hexahedral meshes, the extraordinary edges and vertices usually form a connected network. The respective weight functions obtained from the available smooth mixed B-splines may not have compact support. Therefore, we decompose the weight functions so that the resulting weight functions and basis functions have a compact support and are still polynomials in the parameter space.

In closing, we stress that the proposed construction can be applied to mixed B-splines of arbitrary degrees, although we have studied only quadratic mixed B-splines so far. To this end, it is necessary to extend the introduced mesh refinement scheme for quadratic mixed B-splines to arbitrary degree. In our experience, the details of this refinement are essential for achieving optimal convergence rates. For cubic SB-splines the mixed $C^0/C^1/C^2$ B-splines introduced in Wei et al. [56] appear particularly promising. Moreover, while we presented some mathematical analyses (e.g., proof of linear independence in 1D), further analysis is needed to prove the numerically observed properties of SB-splines. In principle, the proposed construction can also be applied to non-uniform B-splines and extended to surfaces with arbitrary topology, i.e. 2-manifolds in $\mathbb{R}^3$. Non-uniform constructions can, amongst others, significantly simplify the enforcement of essential boundary conditions. In the case of surfaces with arbitrary topology, the SB-splines have to be constructed on a set of intermediate parametric domains corresponding to each of the extraordinary vertices. The so-obtained SB-splines on parametric domains can be subsequently mapped to $\mathbb{R}^3$. Lastly, to make the presented construction useful in geometric design, the introduced new degrees of freedom around the extraordinary features must be associated with control vertex positions. Following related constructions in geometric modelling, see [46,48,64,65,67], this may be achieved by projecting the new degrees of freedom to the existing or possibly some new control vertex positions in the mesh.

Declaration of competing interest

The authors declare that they have no known competing financial interests or personal relationships that could have appeared to influence the work reported in this paper.

Data availability

Data will be made available on request.

Acknowledgments

D. Toshniwal was supported by project number 212.150 funded through the Veni research programme by the Dutch Research Council (NWO).

Appendix A. Linear independence

We provide in this appendix a proof for the linear independence of the one-dimensional SB-splines. We consider as in Figs. 2 and 3 a 1D setup with n_B mixed B-splines $B_i(x)$ of degree $p_B \geq 2$. As discussed in Section 2, we assume that the prescribed B-spline smoothness is C^0 at a single breakpoint and C^{p_B-1} at all others. In general, the mixed B-splines $B_i(x)$ will be non-polynomials in physical space because of the isoparametric mapping, see (2). Let $\mathcal{B}$ denote the set of n_B mixed B-splines $B_i(x)$, $\mathcal{P}$ the set of $n_Q = p_Q + 1$ Bernstein polynomials and $\mathcal{N}$ the set of $n_N = n_B + n_Q$ SB-splines. The set $\mathcal{B}$ is split into the two non-intersecting sets

$$\mathcal{B}^B = \left\{ B_i \mid \text{supp}\, B_i \subset \Omega^Q \right\} \quad \text{and} \quad \mathcal{B}^C = \mathcal{B} \setminus \mathcal{B}^B \,. \tag{A.1}$$

The set $\mathcal{N}$ is composed of the three non-intersecting sets

$$\mathcal{N}^B = \left\{ w^B B_i \mid B_i \in \mathcal{B}^B \right\} \,, \quad \mathcal{N}^Q = \left\{ w^Q Q_i \mid Q_i \in \mathcal{P} \right\} \quad \text{and} \quad \mathcal{N}^C = \mathcal{N} \setminus \left(\mathcal{N}^B \cup \mathcal{N}^Q \right) \,. \tag{A.2}$$

As implied by the choice of weight function in (6), $\nexists B_i \in \mathcal{B}^B$ such that $w^B|_{\text{supp}\, B_i} = 0$, and similarly $\nexists Q_i \in \mathcal{P}$ such that $w^Q|_{\text{supp}\, Q_i} = 0$. We want to prove that the functions in $\mathcal{N}$ are linearly independent.

Linear independence requires that

$$\sum_{N_i \in \mathcal{N}} N_i(x)\alpha_i = 0 \quad \forall x \in \Omega \,, \tag{A.3}$$

is satisfied only when the coefficients $\alpha_i = 0$. Observe that outside the blending domain, (A.3) reduces to

$$\sum_{N_i \in \mathcal{N}^C} N_i(x)\alpha_i = \sum_{B_i \in \mathcal{B}^C} B_i(x)\alpha_i = 0 \quad \forall x \in \Omega \setminus \Omega^Q \,. \tag{A.4}$$

Therefore, due to the linear independence of B-splines, we obtain $\alpha_i = 0$ for all $N_i(x) \in \mathcal{N}^C$. The remaining terms in (A.3) correspond to splines with a support inside the blending region Ω^Q. We prove by contradiction that the coefficients of the non-vanishing terms must be zeros. Assume that the SB-splines are linearly dependent such that

$$\sum_{N_i \in \mathcal{N}^B} N_i(x)\alpha_i = \sum_{N_j \in \mathcal{N}^Q} N_j(x)\alpha_j \quad \forall x \in \Omega^Q \,, \tag{A.5}$$

or equivalently that

$$w^B(x) \sum_{B_i \in \mathcal{B}^B} B_i(x)\alpha_i = \left(1 - w^B(x)\right) \sum_{Q_j \in \mathcal{P}} Q_j(x)\alpha_j \,. \tag{A.6}$$

Next, observe that there are two elements $\Omega_{k1}, \Omega_{k2} \subset \Omega^Q$ such that on each there is only one function from $\mathcal{N}^B$ that is non-zero, e.g., the leftmost or the rightmost element in the grey region in Fig. 2 or Fig. 3. Let the corresponding non-zero functions be N_{i1}, N_{i2}, respectively. Then, we have $w^B|_{\Omega_{k\ell}} = (1 - B_{i\ell})$ and $w^Q|_{\Omega_{k\ell}} = B_{i\ell}$, $\ell = 1, 2$, thus

$$(1 - B_{i\ell}(x))\alpha_{i\ell} = \sum_{Q_j \in \mathcal{P}} Q_j(x)\alpha_j \quad \forall x \in \Omega_{k\ell} \subset \Omega^Q \,, \quad \ell = 1, 2 \,. \tag{A.7}$$

Note that the right hand side is a polynomial function.

- Case 1: Let $B_{i\ell}|_{\Omega_{k\ell}}$ be non-polynomial. Then, the equality in (A.7) can be satisfied only if both sides are equal to 0.
- Case 2: Let the isoparametric mapping be such that both Ω_{k1}, Ω_{k2} are obtained by affinely mapping the associated element in parameter space. Thus, $B_{i\ell}|_{\Omega_{k\ell}}$ are degree p_B polynomials for both $\ell = 1, 2$. This has two implications. First, for equality, both the left and right hand sides in (A.7) need to represent the same polynomial, say f, of degree $p = \min\{p_B, p_Q\}$. Note that f is thus a global polynomial on Ω^Q. Second, by the end-point vanishing property of B-splines, $B_{i\ell}$ vanishes p_B times on one of the endpoints of $\Omega_{k\ell}$, $\ell = 1, 2$. This imposes $2p_B$ constraints on the polynomial f, thus implying $f = 0$.

Both the above cases imply that the right hand side in (A.7) is zero and, in particular, all coefficients of Q_i are thus zero by their linear independence. As a result, the right hand side in (A.6) is zero, thus implying that all coefficients of $B_i \in \mathcal{B}^B$ are zero by their linear independence.

Appendix B. Finite element discretisation

B.1. Poisson equation

The Poisson equation is given by

$$\begin{aligned} -\Delta u &= f && \text{in } \Omega\,, \\ u &= \bar{u} && \text{on } \Gamma_D\,, \\ \nabla u \cdot \boldsymbol{n} &= \bar{t} && \text{on } \Gamma_N\,, \end{aligned} \tag{B.1}$$

where u is the solution field in the domain Ω due to the body force f, $\bar{u}$ is the prescribed solution field on the Dirichlet boundary Γ_D, $\bar{t}$ is the prescribed flux on the Neumann boundary Γ_N with the outward unit normal $\boldsymbol{n}$, ∇ is the gradient operator and $\Delta = \nabla \cdot \nabla$ is the Laplacian operator. The weak formulation of the Poisson equation can be stated as [70,71]: Find $u \in H^1(\Omega)$ such that

$$a(u, v) = l(v)\,, \tag{B.2}$$

for all $v \in H^1(\Omega)$ with

$$a(u, v) = \int_\Omega \nabla u \cdot \nabla v \,\mathrm{d}\Omega + \gamma \int_{\Gamma_D} uv \,\mathrm{d}\Gamma - \int_{\Gamma_D} \Big(u\,(\nabla v \cdot \boldsymbol{n}) + v\,(\nabla u \cdot \boldsymbol{n}) \Big) \,\mathrm{d}\Gamma\,, \tag{B.3a}$$

$$l(v) = \int_\Omega vs \,\mathrm{d}\Omega + \int_{\Gamma_N} v\bar{t} \,\mathrm{d}\Gamma + \gamma \int_{\Gamma_D} v\bar{u} \,\mathrm{d}\Gamma - \int_{\Gamma_D} (\nabla v \cdot \boldsymbol{n})\,\bar{u} \,\mathrm{d}\Gamma\,, \tag{B.3b}$$

and the positive stabilisation parameter γ.

B.2. Biharmonic equation

The biharmonic equation is given by

$$\begin{aligned} \Delta^2 u &= f && \text{in } \Omega\,, \\ u = \bar{u}, \quad \nabla u \cdot \boldsymbol{n} &= \bar{t} && \text{on } \Gamma_D\,, \\ \Delta u = \bar{\kappa}, \quad \nabla(\Delta u) \cdot \boldsymbol{n} &= \bar{\lambda} && \text{on } \Gamma_N\,, \end{aligned} \tag{B.4}$$

where $\bar{\kappa}$ and $\bar{\lambda}$ are respectively the bending moment and shear force prescribed on the Neumann boundary Γ_N. The weak formulation of the biharmonic equation can be stated as [72]: Find $u \in H^2(\Omega)$ such that

$$a(u, v) = l(v)\,, \tag{B.5}$$

for all $v \in H^2(\Omega)$ where

$$\begin{aligned} a(u, v) = &\int_\Omega \Delta u\, \Delta v \,\mathrm{d}\Omega + \gamma \int_{\Gamma_D} uv \,\mathrm{d}\Gamma + \tau \int_{\Gamma_D} (\nabla u \cdot \boldsymbol{n})\,(\nabla v \cdot \boldsymbol{n}) \,\mathrm{d}\Gamma + \int_{\Gamma_D} \Big(u\,(\nabla\,(\Delta v) \cdot \boldsymbol{n}) + v\,(\nabla\,(\Delta u) \cdot \boldsymbol{n}) \Big) \,\mathrm{d}\Gamma \\ &- \int_{\Gamma_D} \Big(\Delta u\,(\nabla v \cdot \boldsymbol{n}) + \Delta v\,(\nabla u \cdot \boldsymbol{n}) \Big) \,\mathrm{d}\Gamma\,, \end{aligned} \tag{B.6a}$$

$$\begin{aligned} l(v) = &\int_\Omega vs \,\mathrm{d}\Omega - \int_{\Gamma_N} v\bar{\lambda} \,\mathrm{d}\Gamma + \int_{\Gamma_N} (\nabla v \cdot \boldsymbol{n})\,\bar{\kappa} \,\mathrm{d}\Gamma + \gamma \int_{\Gamma_D} v\bar{u} \,\mathrm{d}\Gamma + \tau \int_{\Gamma_D} (\nabla v \cdot \boldsymbol{n})\,\bar{t} \,\mathrm{d}\Gamma \\ &+ \int_{\Gamma_D} (\nabla\,(\Delta v) \cdot \boldsymbol{n})\,\bar{u} \,\mathrm{d}\Gamma - \int_{\Gamma_D} (\Delta v)\,\bar{t} \,\mathrm{d}\Gamma\,. \end{aligned} \tag{B.6b}$$

B.3. Finite element discretisation

We discretise the trial and test functions with the SB-splines as

$$u^h(\boldsymbol{x}) = \sum_{i=1}^{n_N} N_i(\boldsymbol{x})\,\alpha_i \quad \text{and} \quad v^h(\boldsymbol{x}) = \sum_{i=1}^{n_N} N_i(\boldsymbol{x})\,\beta_i\,. \tag{B.7}$$

Introducing the interpolation equation (B.7) into the weak form of Poisson equation (B.2) or biharmonic equation (B.5) yields a system of linear equations with the unknowns α_i. For instance, the bilinear form $a(u^h, v^h)$ for the Poisson equation becomes after discretisation

$$a(u^h, v^h) = \sum_{i=1}^{n_N}\sum_{j=1}^{n_N} \alpha_i \left(\int_\Omega \nabla N_i \nabla N_j \,\mathrm{d}\Omega + \gamma \int_{\Gamma_D} N_i N_j \,\mathrm{d}\Gamma - \int_{\Gamma_D} \Big(N_i \left(\nabla N_j \cdot \boldsymbol{n}\right) + N_j \left(\nabla N_i \cdot \boldsymbol{n}\right) \Big) \,\mathrm{d}\Gamma \right) \beta_j\,. \tag{B.8}$$

As usual, the domain integral is evaluated numerically after splitting it into n_{el} element contributions

$$a(u^h, v^h) = \sum_{k=1}^{n_{el}} \left(\sum_{i=1}^{n_N}\sum_{j=1}^{n_N} \alpha_i \left(\int_{\Omega_k} \nabla N_i \nabla N_j \,\mathrm{d}\Omega_k + \gamma \int_{(\Gamma_D)_k} N_i N_j \,\mathrm{d}\Gamma_k - \int_{(\Gamma_D)_k} \Big(N_i \left(\nabla N_j \cdot \boldsymbol{n}\right) + N_j \left(\nabla N_i \cdot \boldsymbol{n}\right) \Big) \,\mathrm{d}\Gamma_k \right) \beta_j \right)\,. \tag{B.9}$$

Appendix C. Mesh refinement

We use for the unstructured quadrilateral mesh the non-nested refinement scheme by Toshniwal [61]. Given a set of mixed B-spline control vertices from the coarse Bézier mesh, the objective is to obtain a new set of mixed B-spline control vertices for defining the refined Bézier mesh. Away from the 1-neighbourhood of an extraordinary vertex, that is, where a tensor product structure is locally present, the knot insertion algorithm is used. The refinement of the 1-neighbourhood of an extraordinary vertex of valence v consists of three steps shown in Fig. C.25. First, the $v \times 3$ mixed B-spline control vertices at the 2-neighbourhood of the refined Bézier mesh are obtained from the knot insertion algorithm as shown in Fig. C.25(a). As a result, only the v mixed B-spline control vertices at the 1-neighbourhood of the refined Bézier mesh remain to be selected. In particular, the remaining v mixed B-spline control vertices are selected such that the v midpoints of the edges at the 1-neighbourhood of the coarse Bézier mesh are interpolated. Therefore, the second step is to estimate the midpoints shown in Fig. C.25(b) using, for instance, a root-finding algorithm together with a parametrisation for the edge length. Subsequently, in the third step a $v \times v$ linear system of equations is solved for the v mixed B-spline control vertices at the 1-neighbourhood of the refined Bézier mesh shown in Fig. C.25(c).

The $v \times v$ linear system is invertible for the case of odd valences $v = 3, 5, \ldots$ but not the case of even valences $v = 6, 8, \ldots$. For even valences, the $v \times v$ linear system has a rank of $v - 1$. For the case of even valences, following [61] we constrain 1 of the v mixed B-spline control vertices so that the $v \times v$ linear system has a unique solution. Evidently, the choice of the constrained mixed B-spline control vertex is not arbitrary. For instance, choosing to constrain a mixed B-spline control vertex that is far away from the extraordinary vertex can distort the refined Bézier mesh. To avoid any mesh distortion, in this paper, we first select 1 of the v extraordinary elements from the coarse Bézier mesh. After that, assuming that the extraordinary vertex is located at the reference element origin $\boldsymbol{\eta} = (0, 0)$ of the selected extraordinary element, we constrain the mixed B-spline control vertex at $\boldsymbol{\eta} = (\eta_1, \eta_2)$ where η_1 and η_2 are decided case by case, i.e. depending on the coarse Bézier mesh. For example, in Section 5.3, we observe that the choice of $\eta_1 = \eta_2$ with $0.125 \leq \eta_1 \leq 0.25$ generally preserves the mesh quality after refinement.

Appendix D. Arbitrary joint and prism valences

We briefly demonstrate that the approach discussed in Section 4.2.2 applies to an extraordinary joint with arbitrary edge valences e and vertex valence v. As a concrete example, Fig. D.26 illustrates the construction of weight functions for an unstructured hexahedral mesh of a truncated box domain with a spherical cavity. The unstructured

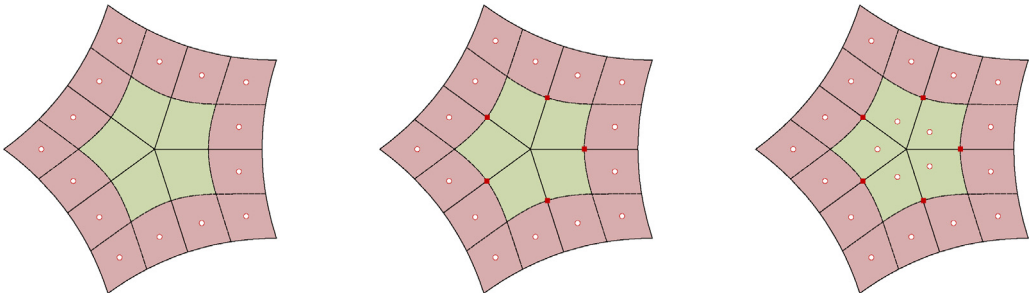

(a) Step 1 of refinement **(b)** Step 2 of refinement **(c)** Step 3 of refinement

Fig. C.25. Refinement of the 1-neighbourhood of an extraordinary vertex with valence $v = 5$. The element boundaries of the coarse and the refined Bézier meshes are depicted as solid line and dashed line, respectively. The refinement scheme consists of three steps. First, the 2-neighbourhood mixed B-spline control vertices of the refined Bézier mesh shown in (a) are obtained using tensor-product knot insertion. Second, we compute the midpoints such that the curve lengths of the 1-neighbourhood edges of the coarse Bézier mesh are approximately bisected shown in (b). Third, the 1-neighbourhood mixed B-spline control vertices of the refined Bézier mesh shown in (c) are computed such that the midpoints determined in (b) are interpolated.

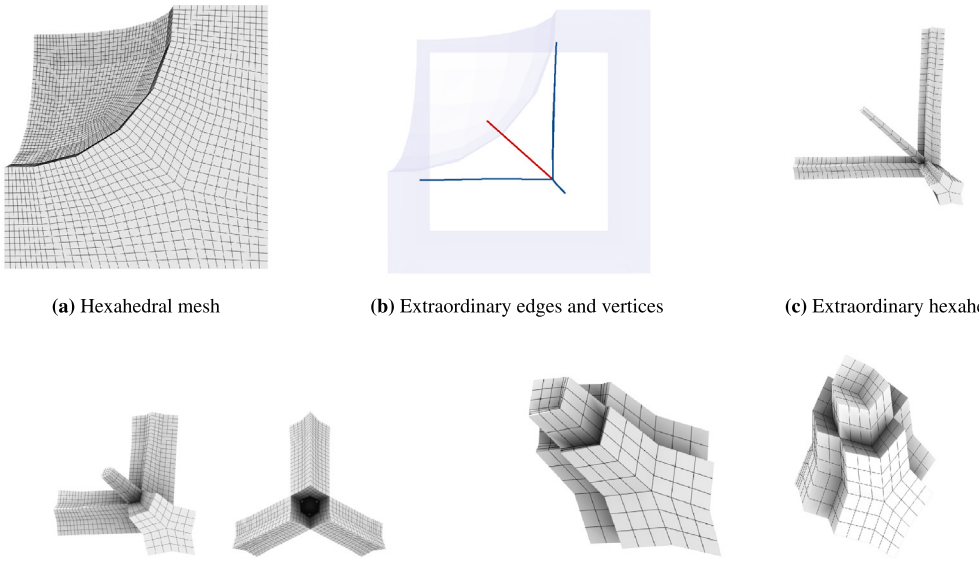

(a) Hexahedral mesh **(b)** Extraordinary edges and vertices **(c)** Extraordinary hexahedra

(d) Extraordinary prisms **(e)** Extraordinary joint and the attached prisms

Fig. D.26. Truncated box domain with a spherical cavity and (a) its discretisation with an unstructured hexahedral mesh, (b) extraordinary edges and vertices of the mesh, (c) extraordinary hexahedra, (d) extraordinary prisms and (e) extraordinary joint and the attached prisms. In (b) the four sets of extraordinary edges of valence $e = 3$ and $e = 5$ are coloured in red and blue, respectively. (For interpretation of the references to colour in this figure legend, the reader is referred to the web version of this article.)

hexahedral mesh shown in Fig. D.26(a) consists of one set of extraordinary edges of valence $e = 3$ and three sets of extraordinary edges of valence $e = 5$ shown in Fig. D.26(b). The valences of the extraordinary edges can be verified from the extraordinary hexahedra of the mesh shown in Fig. D.26(c). Overall, the unstructured hexahedral mesh consists of an extraordinary joint where the extraordinary edges of valence $e = 3$ and $e = 5$ meet at a vertex of valence $v = 10$. As discussed in Section 4.2.2, we first require that the support of the prism weight functions do not overlap at the extraordinary joint, see Fig. D.26(d) depicting the union of the prism weight function supports. Subsequently, the extraordinary joint weight function is defined over the set of hexahedra in Fig. D.26(e).

Conceptually, the extraordinary joint weight function defined over the set of hexahedra in Fig. D.26(e) resembles that shown in Fig. 14(a).

References

[1] P. Fischer, M. Klassen, J. Mergheim, P. Steinmann, R. Müller, Isogeometric analysis of 2D gradient elasticity, Comput. Mech. 47 (3) (2011) 325–334.

[2] S. Rudraraju, A. Van der Ven, K. Garikipati, Three-dimensional isogeometric solutions to general boundary value problems of Toupin's gradient elasticity theory at finite strains, Comput. Methods Appl. Mech. Engrg. 278 (2014) 705–728.

[3] J. Niiranen, S. Khakalo, V. Balobanov, A.H. Niemi, Variational formulation and isogeometric analysis for fourth-order boundary value problems of gradient-elastic bar and plane strain/stress problems, Comput. Methods Appl. Mech. Engrg. 308 (2016) 182–211.

[4] R. de Borst, C.V. Verhoosel, Gradient damage vs phase-field approaches for fracture: Similarities and differences, Comput. Methods Appl. Mech. Engrg. 312 (2016) 78–94.

[5] D. Codony, O. Marco, S. Fernández-Méndez, I. Arias, An immersed boundary hierarchical B-spline method for flexoelectricity, Comput. Methods Appl. Mech. Engrg. 354 (2019) 750–782.

[6] H. Gómez, V.M. Calo, Y. Bazilevs, T.J.R. Hughes, Isogeometric analysis of the Cahn–Hilliard phase-field model, Comput. Methods Appl. Mech. Engrg. 197 (2008) 4333–4352.

[7] L. Dedè, M.J. Borden, T.J.R. Hughes, Isogeometric analysis for topology optimization with a phase field model, Arch. Comput. Methods Eng. 19 (2012) 427–465.

[8] J. Liu, L. Dede, J.A. Evans, M.J. Borden, T.J.R. Hughes, Isogeometric analysis of the advective Cahn–Hilliard equation: spinodal decomposition under shear flow, J. Comput. Phys. 242 (2013) 321–350.

[9] F. Cirak, M. Ortiz, P. Schröder, Subdivision surfaces: A new paradigm for thin-shell finite-element analysis, Internat. J. Numer. Methods Engrg. 47 (2000) 2039–2072.

[10] J. Kiendl, K.-U. Bletzinger, J. Linhard, R. Wüchner, Isogeometric shell analysis with Kirchhoff–Love elements, Comput. Methods Appl. Mech. Engrg. 198 (2009) 3902–3914.

[11] D.J. Benson, Y. Bazilevs, M.-C. Hsu, T.J.R. Hughes, A large deformation, rotation-free, isogeometric shell, Comput. Methods Appl. Mech. Engrg. 200 (13–16) (2011) 1367–1378.

[12] A. Bartezzaghi, L. Dedè, A. Quarteroni, Isogeometric analysis of high order partial differential equations on surfaces, Comput. Methods Appl. Mech. Engrg. 295 (2015) 446–469.

[13] Q. Long, P.B. Bornemann, F. Cirak, Shear-flexible subdivision shells, Internat. J. Numer. Methods Engrg. 90 (2012) 1549–1577.

[14] R. Echter, B. Oesterle, M. Bischoff, A hierarchic family of isogeometric shell finite elements, Comput. Methods Appl. Mech. Engrg. 254 (2013) 170–180.

[15] P. Murdoch, S. Benzley, T. Blacker, S.A. Mitchell, The spatial twist continuum: A connectivity based method for representing all-hexahedral finite element meshes, Finite Elem. Anal. Des. 28 (2) (1997) 137–149.

[16] M. Tarini, K. Hormann, P. Cignoni, C. Montani, PolyCube-Maps, ACM Trans. Graph. 23 (3) (2004) 853–860.

[17] M. Nieser, U. Reitebuch, K. Polthier, CubeCover–parameterization of 3D volumes, Comput. Graph. Forum 30 (2011) 1397–1406.

[18] J.F. Shepherd, C.R. Johnson, Hexahedral mesh generation constraints, Eng. Comput. 24 (3) (2008) 195–213.

[19] Y. Li, Y. Liu, W. Xu, W. Wang, B. Guo, All-hex meshing using singularity-restricted field, ACM Trans. Graph. 31 (2012) 1–11.

[20] Y.J. Zhang, Geometric Modeling and Mesh Generation from Scanned Images, Chapman and Hall/CRC, 2018.

[21] M. Bracci, M. Tarini, N. Pietroni, M. Livesu, P. Cignoni, Hexalab.net: An online viewer for hexahedral meshes, Comput. Aided Des. 110 (2019) 24–36.

[22] P. Zhang, J. Vekhter, E. Chien, D. Bommes, E. Vouga, J. Solomon, Octahedral frames for feature-aligned cross fields, ACM Trans. Graph. 39 (3) (2020) 1–13.

[23] M. Livesu, N. Pietroni, E. Puppo, A. Sheffer, P. Cignoni, LoopyCuts: practical feature-preserving block decomposition for strongly hex-dominant meshing, ACM Trans. Graph. 39 (4) (2020) 121:1–121:17.

[24] T.D. DeRose, Necessary and sufficient conditions for tangent plane continuity of Bézier surfaces, Comput. Aided Geom. Design 7 (1–4) (1990) 165–179.

[25] U. Reif, TURBS—topologically unrestricted rational B-splines, Constr. Approx. 14 (1998) 57–77.

[26] M.A. Scott, D.C. Thomas, E.J. Evans, Isogeometric spline forests, Comput. Methods Appl. Mech. Engrg. 269 (2014) 222–264.

[27] T. Nguyen, K. Karčiauskas, J. Peters, C^1 finite elements on non-tensor-product 2D and 3D manifolds, Appl. Math. Comput. 272 (2016) 148–158.

[28] A. Collin, G. Sangalli, T. Takacs, Analysis-suitable G^1 multi-patch parametrizations for C^1 isogeometric spaces, Comput. Aided Geom. Design 47 (2016) 93–113.

[29] D. Toshniwal, H. Speleers, T.J.R. Hughes, Smooth cubic spline spaces on unstructured quadrilateral meshes with particular emphasis on extraordinary points: Geometric design and isogeometric analysis considerations, Comput. Methods Appl. Mech. Engrg. 327 (2017) 411–458.

[30] D. Toshniwal, H. Speleers, R.R. Hiemstra, T.J.R. Hughes, Multi-degree smooth polar splines: A framework for geometric modeling and isogeometric analysis, Comput. Methods Appl. Mech. Engrg. 316 (2017) 1005–1061.

[31] M. Kapl, F. Buchegger, M. Bercovier, B. Jüttler, Isogeometric analysis with geometrically continuous functions on planar multi-patch geometries, Comput. Methods Appl. Mech. Engrg. 316 (2017) 209–234.

[32] M. Kapl, G. Sangalli, T. Takacs, Construction of analysis-suitable G^1 planar multi-patch parameterizations, Comput. Aided Des. 97 (2018) 41–55.

[33] K. Karčiauskas, J. Peters, Multi-sided completion of C^2 bi-3 and C^1 bi-2 splines: A unifying approach, Comput. Aided Geom. Design 86 (2021) 101978.
[34] D. Doo, M.A. Sabin, Behavior of recursive division surfaces near extraordinary points, Comput. Aided Des. 10 (1978) 356–360.
[35] E. Catmull, J. Clark, Recursively generated B-spline surfaces on arbitrary topological meshes, Comput. Aided Des. 10 (1978) 350–355.
[36] J. Peters, U. Reif, Subdivision Surfaces, Springer, 2008.
[37] X. Wei, Y.J. Zhang, T.J.R. Hughes, M.A. Scott, Truncated hierarchical Catmull–Clark subdivision with local refinement, Comput. Methods Appl. Mech. Engrg. 291 (2015) 1–20.
[38] X. Wei, X. Li, Y.J. Zhang, T.J.R. Hughes, Tuned hybrid nonuniform subdivision surfaces with optimal convergence rates, Internat. J. Numer. Methods Engrg. 122 (9) (2021) 2117–2144.
[39] Q. Zhang, M. Sabin, F. Cirak, Subdivision surfaces with isogeometric analysis adapted refinement weights, Comput. Aided Des. 102 (2018) 104–114.
[40] Y. Ma, W. Ma, A subdivision scheme for unstructured quadrilateral meshes with improved convergence rate for isogeometric analysis, Graph. Models 106 (2019) 101043.
[41] R. Clough, J. Tocher, Finite element stiffness matricess for analysis of plate bending, in: Proceedings of the Conference on Matrix Methods in Structuraly Analysis, 1965, pp. 515–546.
[42] M.J.D. Powell, M.A. Sabin, Piecewise quadratic approximations on triangles, ACM Trans. Math. Software 3 (1977) 316–325.
[43] M.-J. Lai, L.L. Schumaker, Spline Functions on Triangulations, Vol. 110, Cambridge University Press, 2007.
[44] C.M. Grimm, J.F. Hughes, Modeling surfaces of arbitrary topology using manifolds, in: SIGGRAPH 1995 Conference Proceedings, 1995, pp. 359–368.
[45] G. Della Vecchia, B. Jüttler, M.-S. Kim, A construction of rational manifold surfaces of arbitrary topology and smoothness from triangular meshes, Comput. Aided Geom. Design 25 (2008) 801–815.
[46] L. Ying, D. Zorin, A simple manifold-based construction of surfaces of arbitrary smoothness, in: SIGGRAPH 2004 Conference Proceedings, ACM Trans. Graph. 23 (2004) 271–275.
[47] E. Tosun, D. Zorin, Manifold-based surfaces with boundaries, Comput. Aided Geom. Design 28 (2011) 1–22.
[48] M. Majeed, F. Cirak, Isogeometric analysis using manifold-based smooth basis functions, Comput. Methods Appl. Mech. Engrg. 316 (2017) 547–567.
[49] Q. Zhang, F. Cirak, Manifold-based isogeometric analysis basis functions with prescribed sharp features, Comput. Methods Appl. Mech. Engrg. 359 (2020) 112659.
[50] Q. Zhang, T. Takacs, F. Cirak, Manifold-based B-splines on unstructured meshes, in: Conference on Isogeometric Analysis and Applications, Springer, 2018, pp. 243–262.
[51] C. Bajaj, S. Schaefer, J. Warren, G. Xu, A subdivision scheme for hexahedral meshes, Vis. Comput. 18 (2002) 343–356.
[52] Y.-S. Chang, K.T. McDonnell, H. Qin, A new solid subdivision scheme based on box splines, in: Proceedings of the Seventh ACM Symposium on Solid Modeling and Applications, 2002, pp. 226–233.
[53] J. Xie, J. Xu, Z. Dong, G. Xu, C. Deng, B. Mourrain, Y.J. Zhang, Interpolatory Catmull-Clark volumetric subdivision over unstructured hexahedral meshes for modeling and simulation applications, Comput. Aided Geom. Design 80 (2020) 101867:1–101867:16.
[54] U. Reif, M.A. Sabin, Old problems and new challenges in subdivision, J. Comput. Appl. Math. 349 (2019) 523–531.
[55] J. Peters, Refinable tri-variate C^1 splines for box-complexes including irregular points and irregular edges, Comput. Aided Geom. Design 80 (2020) 101877.
[56] X. Wei, Y.J. Zhang, D. Toshniwal, H. Speleers, X. Li, C. Manni, J.A. Evans, T.J.R. Hughes, Blended B-spline construction on unstructured quadrilateral and hexahedral meshes with optimal convergence rates in isogeometric analysis, Comput. Methods Appl. Mech. Engrg. 341 (2018) 609–639.
[57] T. Schneider, J. Dumas, X. Gao, M. Botsch, D. Panozzo, D. Zorin, Poly-spline finite-element method, ACM Trans. Graph. 38 (3) (2019) 1–16.
[58] T. Schneider, D. Panozzo, X. Zhou, Isogeometric high order mesh generation, Comput. Methods Appl. Mech. Engrg. 386 (2021) 114104.
[59] D. Wang, H. Zhang, A consistently coupled isogeometric–meshfree method, Comput. Methods Appl. Mech. Engrg. 268 (2014) 843–870.
[60] E. Febrianto, M. Ortiz, F. Cirak, Mollified finite element approximants of arbitrary order and smoothness, Comput. Methods Appl. Mech. Engrg. 373 (2021) 113513.
[61] D. Toshniwal, Quadratic splines on quad-tri meshes: Construction and an application to simulations on watertight reconstructions of trimmed surfaces, Comput. Methods Appl. Mech. Engrg. 388 (2022) 114174.
[62] J.M. Melenk, I. Babuška, The partition of unity finite element method: basic theory and applications, Comput. Methods Appl. Mech. Engrg. 139 (1996) 289–314.
[63] F. Buchegger, B. Jüttler, A. Mantzaflaris, Adaptively refined multi-patch B-splines with enhanced smoothness, Appl. Math. Comput. 272 (2016) 159–172.
[64] D. Zorin, Constructing curvature-continuous surfaces by blending, in: Proceedings of the Fourth Eurographics Symposium on Geometry Processing, 2006, pp. 31–40.
[65] A. Levin, Modified subdivision surfaces with continuous curvature, in: SIGGRAPH 2006 Conference Proceedings, 2006, pp. 1035–1040.
[66] N. Pla-Garcia, M. Vigo-Anglada, J. Cotrina-Navau, N-sided patches with B-spline boundaries, Comput. Graphics 30 (2006) 959–970.
[67] M. Antonelli, C.V. Beccari, G. Casciola, R. Ciarloni, S. Morigi, Subdivision surfaces integrated in a CAD system, Comput. Aided Des. 45 (2013) 1294–1305.
[68] Y. Bazilevs, L. Beirao de Veiga, J.A. Cottrell, T.J.R. Hughes, G. Sangalli, Isogeometic analysis: approximation, stability and error estimates for h-refined meshes, Math. Methods Models Appl. Sci. 16 (2006) 1031–1090.

[69] A. Tagliabue, L. Dedè, A. Quarteroni, Isogeometric analysis and error estimates for high order partial differential equations in fluid dynamics, Comput. & Fluids 102 (2014) 277–303.
[70] J. Nitsche, Über ein variationsprinzip zur lösung von Dirichlet-problemen bei verwendung von teilräumen, die keinen randbedingungen unterworfen sind, Abh. Math. Semin. Univ. Hambg. 36 (1971) 9–15.
[71] S. Fernandez-Mendez, A. Huerta, Imposing essential boundary conditions in mesh-free methods, Comput. Methods Appl. Mech. Engrg. 193 (2004) 1257–1275.
[72] A. Embar, J. Dolbow, I. Harari, Imposing Dirichlet boundary conditions with Nitsche's method and spline-based finite elements, Internat. J. Numer. Methods Engrg. 83 (7) (2010) 877–898.